

Discontinuous Igneous Addition along the Eastern North American Margin beneath the East Coast Magnetic Anomaly

Collin Brandl¹, Lindsay L. Worthington¹, Maria Beatrice Magnani², Donna Shillington³, and Thomas W Luckie⁴

¹University of New Mexico

²Southern Methodist University

³Northern Arizona University

⁴University of Southern California

February 20, 2023

Abstract

Detailed models of crustal structure at volcanic passive margins offer insight into the role of magmatism and distribution of igneous addition during continental rifting. The Eastern North American Margin (ENAM) is a volcanic passive margin that formed during the breakup of Pangea ~200 Myr ago. The offshore, margin-parallel East Coast Magnetic Anomaly (ECMA) is thought to mark the locus of synrift magmatism. Previous widely spaced margin-perpendicular studies seismically imaged igneous addition as seaward dipping reflectors (SDRs) and high velocity lower crust (HVLC; >7.2 km/s) beneath the ECMA. Along-strike imaging is necessary to more accurately determine the distribution and volume of igneous addition during continental breakup. We use wide-angle, marine active-source seismic data from the 2014-2015 ENAM Community Seismic Experiment to determine crustal structure beneath a ~370-km-long section of the ECMA. P-wave velocity models based on data from short-period ocean bottom seismometers reveal a ~21-km-thick crust with laterally variable lower crust velocities ranging from 6.9 to 7.5 km/s. Sections with HVLC alternate with two ~30-km-wide areas where the velocities do not exceed 7.0 km/s. This variable structure indicates that HVLC is discontinuous along the margin. Velocity-thickness analysis indicates that the HVLC discontinuity is the result of variable intrusion along-strike. Our results suggest that magmatism during early rifting was segmented and was lower in volume than previously thought. The HVLC discontinuities roughly align with locations of Mid-Atlantic Ridge fracture zones, which may indicate that early rift segmentation influenced later segmentation of the Mid-Atlantic Ridge.

1 **Discontinuous Igneous Addition along the Eastern North American**
2 **Margin beneath the East Coast Magnetic Anomaly**

3 **Collin C. Brandl¹, Lindsay Lowe Worthington¹, Maria Beatrice Magnani²,**
4 **Donna J. Shillington³, Thomas W. Luckie⁴**

5
6 ¹ Department of Earth and Planetary Sciences, The University of New Mexico,
7 Albuquerque, New Mexico 87131, USA

8 ² Department of Earth Sciences, Southern Methodist University, Dallas, Texas 75275,
9 USA

10 ³ School of Earth and Sustainability, Northern Arizona University, Flagstaff, Arizona
11 86011, USA

12 ⁴ Department of Earth Sciences, University of Southern California, Los Angeles,
13 California 90089, USA

14 Corresponding author: Collin Brandl (cbrandl@unm.edu)

15 Key Points:

- 16 - High velocity lower crust beneath the East Coast Magnetic Anomaly is
17 discontinuous and represents magmatic segmentation during rifting
- 18 - The extrusive:intrusive ratio at the ENAM is lower than the global average
19 resulting in a significantly reduced total igneous volume
- 20 - The HVLC discontinuities are coincident to Mid-Atlantic Ridge fracture zones,
21 potentially indicating a rift to ridge connection

22

23 **Abstract**

24 Detailed models of crustal structure at volcanic passive margins offer insight into the
25 role of magmatism and distribution of igneous addition during continental rifting. The
26 Eastern North American Margin (ENAM) is a volcanic passive margin that formed during
27 the breakup of Pangea ~200 Myr ago. The offshore, margin-parallel East Coast
28 Magnetic Anomaly (ECMA) is thought to mark the locus of synrift magmatism. Previous
29 widely spaced margin-perpendicular studies seismically imaged igneous addition as
30 seaward dipping reflectors (SDRs) and high velocity lower crust (HVLC; >7.2 km/s)
31 beneath the ECMA. Along-strike imaging is necessary to more accurately determine the
32 distribution and volume of igneous addition during continental breakup. We use wide-
33 angle, marine active-source seismic data from the 2014-2015 ENAM Community
34 Seismic Experiment to determine crustal structure beneath a ~370-km-long section of
35 the ECMA. P-wave velocity models based on data from short-period ocean bottom
36 seismometers reveal a ~21-km-thick crust with laterally variable lower crust velocities
37 ranging from 6.9 to 7.5 km/s. Sections with HVLC alternate with two ~30-km-wide areas
38 where the velocities do not exceed 7.0 km/s. This variable structure indicates that HVLC
39 is discontinuous along the margin. Velocity-thickness analysis indicates that the HVLC
40 discontinuity is the result of variable intrusion along-strike. Our results suggest that
41 magmatism during early rifting was segmented and was lower in volume than previously
42 thought. The HVLC discontinuities roughly align with locations of Mid-Atlantic Ridge
43 fracture zones, which may indicate that early rift segmentation influenced later
44 segmentation of the Mid-Atlantic Ridge.

45 **Plain Language Summary**

46 The East Coast of the United States is a passive margin that formed during continental
47 breakup of Pangea, the most recent supercontinent. Although passive margins are
48 generally not locales of active faulting and magmatism, by investigating their current
49 structure, we gain insight into processes during past rifting. We know that extensive
50 volcanism and magmatic addition to the Earth's crust occurred during the breakup of
51 Pangea, but we do not fully understand how the distribution changes from north to south
52 along the margin. To study these rocks, which are buried 10 – 20 km beneath the
53 seafloor, we use ocean bottom seismometers that record human made sound waves to
54 determine the sound speed of rocks beneath the surface, which depends on the specific
55 type of rock. We found that the thickness and extent of magma-derived rocks are
56 variable along the margin, with gaps up to 30 km wide. We think that the variability of
57 these rocks is related to processes happening in the continental rift, and that it may
58 have influenced the structure of the Mid-Atlantic Ridge that formed after rifting ended.
59 We also estimate that the total volume of igneous rocks emplaced during breakup is
60 significantly less than previously thought.

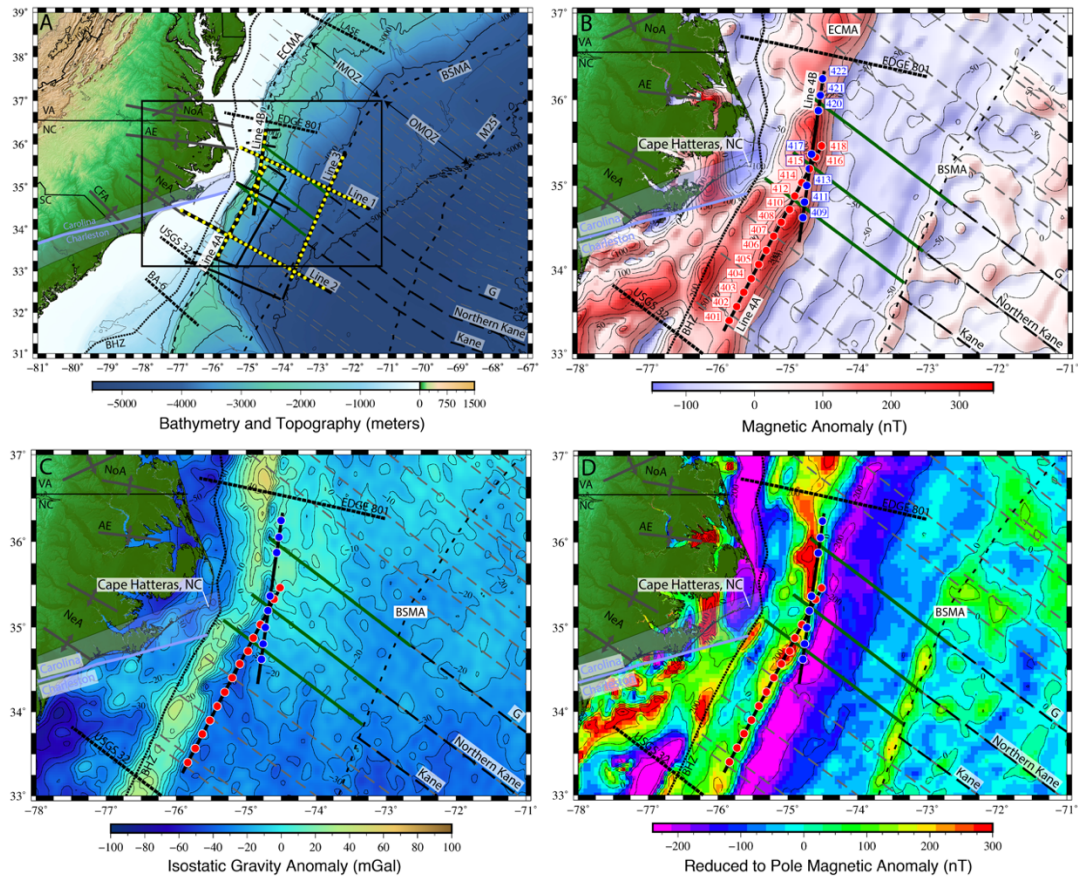
61 **1. Introduction**

62 Volcanic passive margins host significant volumes of igneous addition that are
63 important not only for promoting continental rifting (Bialas et al., 2010; Geoffroy et al.,
64 2015; Thybo & Nielsen, 2009), but also for global environment change and mass
65 extinction events (Marzoli et al., 2018) and the understanding of mantle conditions and
66 processes (e.g. Korenaga et al., 2002; Shuck et al., 2019). The volume and distribution
67 of magmatism and its partitioning between the upper and lower crust during rifting is
68 poorly known because there are limited datasets available to constrain 3D structure at

69 sites of breakup. Along-strike variability in margin structure can offer insight into syn-rift
70 processes and potential connections between margin and mid-ocean ridge
71 segmentation. Strike-perpendicular seismic imaging has constrained along-strike
72 variability at passive margins on larger scales (e.g., Aslanian et al., 2021; Becker et al.,
73 2014; Faleide et al., 2008; Holbrook & Kelemen, 1993; Klingelhoefer et al., 2009;
74 Koopmann et al., 2014), but the paucity of along-strike imaging has prevented the
75 necessary understanding of changes in crustal structure and magmatism along rifts.

76 The Eastern North American Margin (ENAM) is a volcanic passive margin that
77 formed during the breakup of Pangea and opening of the Atlantic Ocean starting at
78 ~200 Ma (Klitgord & Schouten, 1986) (Fig. 1). Crustal structure of the ENAM reflects the
79 conditions of continental breakup, with records of extension and magmatism frozen into
80 the current lithospheric structure. The ENAM has been considered an archetype for
81 volcanic margins based on strike-perpendicular crustal structure containing seaward
82 dipping reflectors (SDRs) and high velocity lower crust (HVLC; >7.2 km/s), which are
83 both interpreted as igneous addition to the margin during rifting (e.g., Austin et al., 1990;
84 Bécél et al., 2020; Holbrook & Kelemen, 1993; Shuck et al., 2019). The East Coast
85 Magnetic Anomaly (ECMA), a large, positive amplitude anomaly that follows the ENAM
86 from Florida to Nova Scotia, is sourced from the volcanic SDR package in the upper
87 crust and has been interpreted as the rift-to-drift transition separating continental and
88 oceanic crust (Alsop & Talwani, 1984; Behn & Lin, 2000; Davis et al., 2018; Greene et
89 al., 2017) (Fig. 1). Along-strike variations in the width and amplitude of the ECMA
90 suggest corresponding changes in rift structure and magmatism, potentially related to

91 segmentation of the Mid-Atlantic Ridge (Behn & Lin, 2000; Greene et al., 2017, 2020)
92 (Fig. 1).



93 **Figure 1) Maps of the ENAM CSE study area with regional geologic and geophysical features.**
94 *A)* Bathymetry and topography shown with the full ENAM CSE survey. Multichannel seismic
95 reflection lines are shown by black solid lines, short period ocean bottom seismometer deployments
96 are shown by yellow circles, and legacy seismic experiment lines EDGE-801, BA-6, USGS 32 and
97 LASE are shown as black labeled lines. Fracture zone extrapolations of Klitgord and Schouten
98 (1986) are shown as gray dashed lines and interpreted inner magnetic quiet zone offsets from
99 Greene et al. (2017) are shown as green lines. Anomaly M25, the Blake Spur Magnetic Anomaly
(BSMA), the Inner Magnetic Quiet Zone (IMQZ), and the Outer Magnetic Quiet Zone (OMQZ) are
labeled. Onshore basement arches and the Carolina-Charleston terrane boundary are labeled. Black
box represents the extent of the other maps. *B)* Zoom in on lines 4A and 4B of the survey with OBS
instrument number labeled. Map shows EMAG2V3 (Meyer et al., 2017). *C)* Isostatic Gravity Anomaly
(Behn and Lin, 2000). *D)* Reduced to Pole (RTP) magnetic anomaly (Behn and Lin, 2000).

100 In this study, we use traveltome tomography to model the P-wave velocity
101 structure beneath the ECMA for a ~370-km-long along-strike section centered on Cape
102 Hatteras, North Carolina. These models and subsequent analyses based on the velocity

103 structure offer insight into the crust beneath the ECMA and delineate along-strike
104 variability in crustal structure at scales of ~30 km which reflect early rifting structures.

105 **1.1 Synrift Magmatism**

106 Igneous addition at continental rifts is often characterized by extensive surface
107 volcanism with localized intrusions into the crust or underplating at the base of the crust
108 (Bastow & Keir, 2011; Ebinger & Casey, 2001; Keranen et al., 2004; Thybo &
109 Artemieva, 2013). Synrift magmatism accommodates some extensional strain during
110 breakup and may be necessary for rifting, as modeling indicates that plate boundary
111 forces alone are too weak to break apart intact continental lithosphere (Bialas et al.,
112 2010; Buck, 2006). Igneous addition at volcanic margins, including the ENAM, the West
113 African Conjugate Margin, the southern West African Margin, and the South American
114 Margin, has been interpreted as a combination of volcanic flows (i.e., the SDRs) and
115 magmatic intrusions or underplating (i.e., the HVLC) (e.g., Aslanian et al., 2021; Becker
116 et al., 2014; Faleide et al., 2008; Holbrook & Kelemen, 1993; Klingelhoefer et al., 2009;
117 Koopmann et al., 2014).

118 Previous studies of the ENAM interpolated between widely spaced margin-
119 perpendicular profiles and assumed long wavelength (100 - >1000 km) along-strike
120 variability of crustal structure (Holbrook & Kelemen, 1993). However, smaller
121 wavelength (<100 km) variability in the magnitude and width of the ECMA implies that
122 there is significant variability in the thickness and extent of the anomaly's source body,
123 thought to be the SDR package, on smaller scales (Behn & Lin, 2000; Davis et al.,
124 2018; Greene et al., 2020). Recent magnetic modeling along the whole margin
125 interpreted multiple scales of magmatic segmentation along the margin based on

126 variability of the SDR package (Greene et al., 2020) (Fig. 1). In the vicinity of Cape
127 Hatteras, NC, the magnetic source body changes broadly from thinner and wider in the
128 south to thicker and narrower to the north, implying that Cape Hatteras is an important
129 boundary along the margin (Greene et al., 2020). Constraining the full crustal structure
130 beneath the ECMA has been difficult because there has been a lack of along-strike
131 imaging at the ENAM and magnetic modeling does not offer insight into the lower crust.
132 Along-strike imaging can illuminate variabilities in the lower crust at similar scales to
133 those in the upper crust observed by whole margin modeling; if the SDRs and the HVLC
134 were connected by the same magmatic plumbing system, we would expect significant
135 variability in the thickness and extent of the HVLC correlated with SDR variability.

136 **1.2 Segmentation of the ENAM**

137 The relationship between segmentation of continental rifts and mature mid-ocean
138 ridges remains unclear, but the crustal structure at rifted margins may hold crucial
139 evidence that that connects them (Behn & Lin, 2000; Gerya, 2013; Greene et al., 2017;
140 Illsley-Kemp et al., 2018; Taylor et al., 2009; Thomas, 2006). Continental rifts exhibit
141 magmatic segmentation with sporadic intrusion and volcanism and/or structural
142 segmentation with distinct fault systems (e.g., Ebinger & Casey, 2001; Hammond et al.,
143 2011; Hayward & Ebinger, 1996). Mid-ocean ridge systems have characteristic
144 segmentation with spreading segments bounded by oceanic transform faults that
145 become fracture zones away from the ridge axis (Schouten et al., 1985). Rift
146 segmentation may carry over to mature spreading centers based on the long
147 wavelength variability of margin anomalies (Behn & Lin, 2000; Wyer & Watts, 2006),
148 modeling of fracture zone formation (Gerya, 2013; Illsley-Kemp et al., 2018; Taylor et

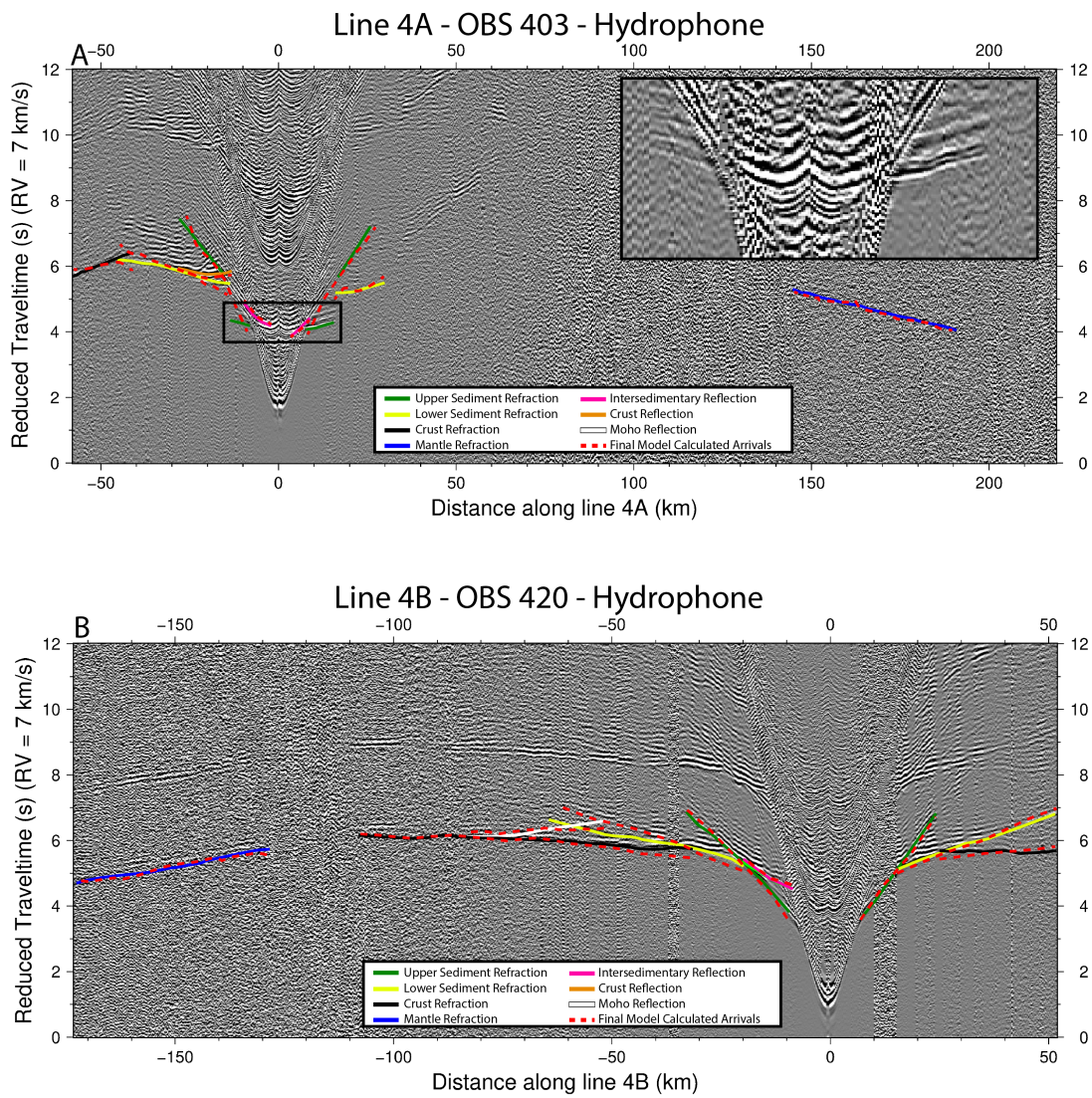
149 al., 1995), structural correlation through multiple Wilson cycles (Thomas, 2006), or
150 correlation between onshore and offshore structures (e.g., Franke et al., 2007;
151 Koopmann et al., 2014).

152 The ECMA magnetic signature shows segmentation at multiple wavelengths
153 (~600 – 1000 km and ~50 – 100 km) that may correlate with Mid-Atlantic Ridge
154 segmentation (Greene et al., 2020). Along-strike segmentation of the SDR package
155 interpreted in the south Atlantic margins and variability observed in the West African
156 Coast Magnetic Anomaly also suggest a connection (Biari et al., 2017; Franke et al.,
157 2007; Klingelhoefer et al., 2009; Koopmann et al., 2014). Relating structures along the
158 ENAM to Mid-Atlantic Ridge segmentation is difficult because of the Atlantic Jurassic
159 Quiet Zone, a region between M25 and the ECMA with no observable seafloor magnetic
160 lineations (Behn & Lin, 2000; Greene et al., 2017) (Fig. 1). The combined lack of
161 lineations and thicker abyssal sediments prevent tracing of Mid-Atlantic Ridge fracture
162 zones in this region, so linear extrapolations based on plate motion have been used to
163 approximate their locations at the ECMA (Behn & Lin, 2000). Recent analysis of the
164 Inner Magnetic Quiet Zone (IMQZ) found faint lineations with offset that correspond to
165 some extrapolated fracture zones, suggesting that there may be some segmentation
166 structures at the ECMA that could be seismically imaged (Greene et al., 2017) (Fig. 1).
167 Shuck et al. (2019) found no correlated structures along the Blake Spur Magnetic
168 Anomaly, an indication that segmentation of the Mid-Atlantic Ridge may have developed
169 after full lithospheric rupture. Previous to our study, magmatic segmentation at the
170 ECMA was implied by Greene et al. (2020), but it remains unclear whether this early
171 segmentation is recorded in the lower crustal structure.

172 **2. Data and Methods**

173 **2.1 ENAM-CSE Line 4A and 4B**

174 For this study we used ocean bottom seismometer (OBS) data from 23 stations
175 acquired as part of the NSF-funded Eastern North American Margin Community
176 Seismic Experiment (ENAM-CSE) in 2014 (Van Avendonk, 2015; Lynner et al., 2019).
177 The OBSs recorded shots from the 36-element, 6600-in³ array of the *R/V Marcus G.*
178 *Langseth* along each profile (Fig. 1). We focus on Lines 4A and 4B located within the
179 peak of the ECMA following the margin along-strike for ~370 km (Fig. 1). OBS gathers
180 used for this study generally have a high signal to noise ratio with multiple arrivals
181 evident and energy arriving from up to ~200 km offsets (Fig. 2). Stations A401-A406
182 have more complex arrivals within short offsets (< +-40 km) and have a near-offset first
183 arrival with an apparent velocity of 6 km/s (much faster than typical sediment velocities)
184 (Fig. 2). Picking arrivals between ~40 km and ~125 km source-receiver offset on
185 stations A401-A406 was difficult due to low amplitudes and low coherency (Fig. 2). We
186 attempted to include these arrivals in the inversions, but it was difficult to distinguish
187 consistent phases and corresponding layer geometry, so only the first arriving, high
188 energy phases were included in this area (Fig. 2). At offsets greater than ~125 km on
189 these OBSs, amplitudes and coherency returned to normal levels and arrivals could be
190 identified and picked (Fig. 2).



191
192
193
194

Figure 2) **Annotated ocean bottom seismometer data.** An OBS gather from Line 4A (station 403) (A) and Line 4B (station 420) (B) of the ENAM CSE plotted in distance along the line and reduced traveltime (with reduction velocity of 7 km/s). Traveltime picks (multicolor - see legend) and final calculated arrivals (red dashed) are plotted on top of data. Inset is an unpicked zoom onto the early, fast arrival caused by salt diapirism found on the southern end of line 4A.

195
196
197
198
199

We used a Butterworth bandpass filter on the OBS gathers to target frequencies between 4 and 15 Hz for general phase identification and interpretation, and between 10 and 25 Hz for near offset reflections. We identified seven phases for use in the velocity inversion that are similar to other recent refraction studies from the ENAM-CSE (i.e., Shuck et al., 2019), including an upper sedimentary refraction (Ps1), a lower

200 sedimentary refraction (Ps2), a crustal refraction (Pg), an upper mantle refraction (Pn),
201 an inter-sedimentary reflection (PsP), a reflection from the top of the crust (PgP), and a
202 Moho reflection (PmP). Uncertainties were assigned to all picked arrivals, ranging from
203 75 – 125 ms, based on source-receiver offset and visual inspection of signal-to-noise
204 ratio. We used forward modeling of picks from each station and verified arrival
205 reciprocity to quality control our traveltimes before inversion.

206 **2.2 Traveltime Tomography**

207 We performed traveltimes tomography with VMTomo following the methods of
208 Van Avendonk et al. (2004) to iteratively invert our traveltimes picks for subsurface P-
209 wave velocities and boundary layer geometry. Our simple starting velocity models were
210 based on results from crossing Lines 1 and 2 (Shuck et al., 2019) taken at the
211 intersection points with Lines 4A and 4B and hung from the seafloor (Suppl. Fig. 1).

212 VMTomo first calculates raypaths and their respective traveltimes for each phase
213 per shot point-OBS pair. The calculated travel times are compared to the corresponding
214 picked traveltimes, and the inversion then seeks to minimize the travel time residual by
215 updating the velocity structure. The models were both constructed with 0.5 km by 0.2
216 km grid cells with no depth dependent changes in size. We chose a raytracing search
217 radius of 0.2 km to match the vertical grid size and prescribed a regularization area of
218 20 km by 0.4 km with higher relative smoothing and a balanced regularization between
219 boundary depths and velocities. In our analyses, the χ^2 error metric was decreased by
220 ~50% with each iteration until a value of ~1 (indicating that the model misfit matches the
221 prescribed uncertainty) was reached. We chose to apply a layer stripping approach,
222 where we first inverted the shallowest layer to a χ^2 of 1 then moved to the next deepest

223 layer while holding everything above fixed. We verified the χ^2 of the entire model by
224 running a final iteration with every phase at once.

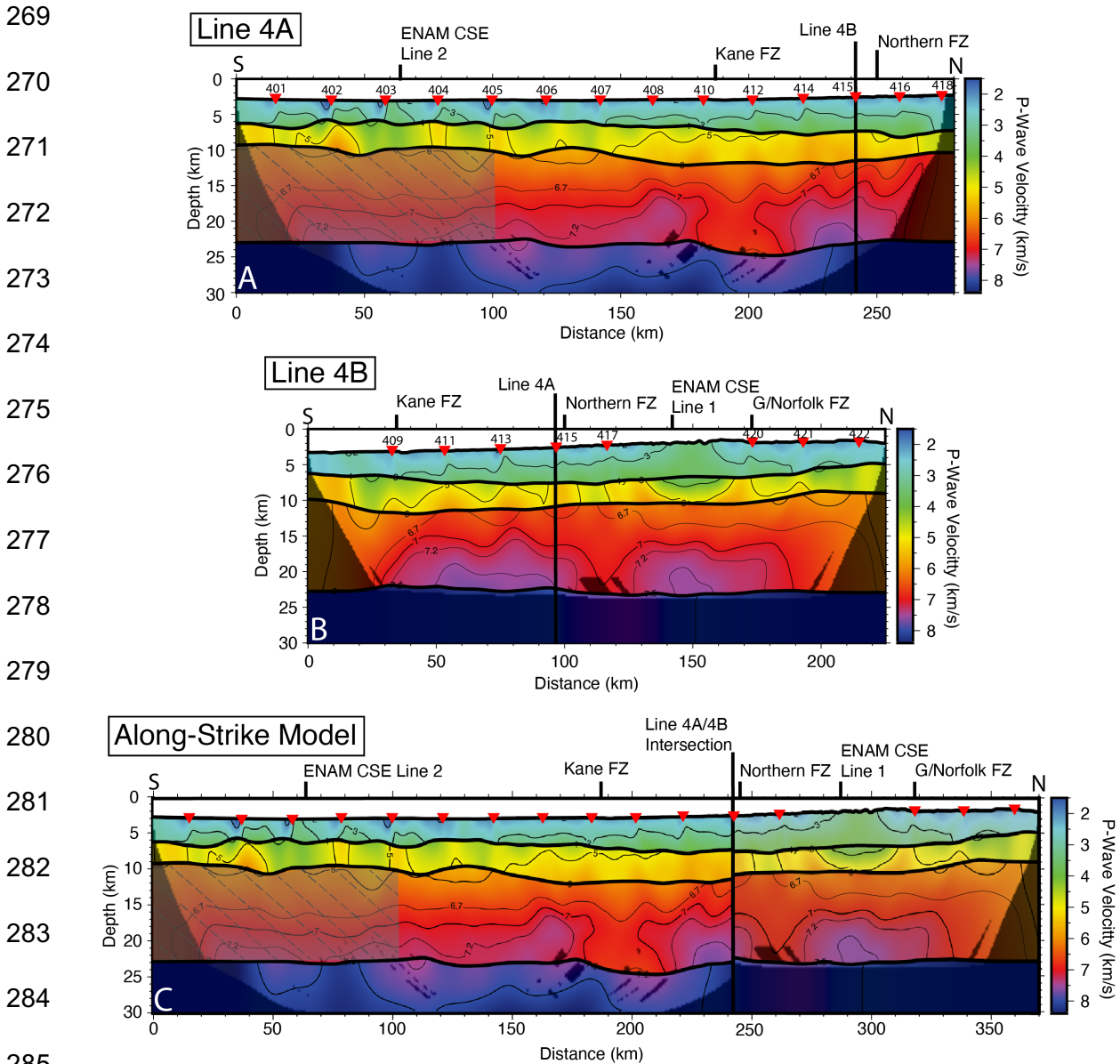
225 We performed resolution tests and calculated derivative weight sum (DWS) on
226 both velocity models to help guide our interpretations (Suppl. Figs. 2,4,5,6). Resolution
227 results greater than ~50% for a given size test ellipse are considered acceptable for
228 active source tomography of this kind (Van Avendonk et al., 2004). With the ray
229 coverage for each line, the velocity models can reliably resolve large scale features
230 (represented by an ellipse of 60 km by 8 km) on both lines within the sedimentary and
231 crust layers except for the region between 0 and 100 km along Line 4A that has
232 significantly low ray coverage (Suppl. Figs. 2,6). The velocity models can also reliably
233 resolve small (10-km wide by 2-km tall) and medium scale features (30-km wide by 5-
234 km tall) in the sedimentary layers and can resolve medium scale features in the crustal
235 layer (Suppl. Figs. 4,5).

236 We estimated the uncertainty in our modeled crustal velocities and in the Moho
237 velocity-depth tradeoff by perturbing our final model, raytracing the corresponding
238 phases, and calculating a new χ^2 . The crustal velocities have acceptable χ^2 values (\leq
239 1.25) with perturbations from -0.05 – 0.07 km/s (Line 4A) and from -0.06 – 0.045 km/s
240 (Line 4B) (Suppl. Figs. 7,8). For the velocity-depth tradeoff, the Moho reflection phase
241 (PmP) has acceptable χ^2 values (\leq 1.25) with depth perturbations from -0.28 – 0.85 km
242 (Line 4A) and -1.5 – 0.78 km (Line 4B) and with velocity perturbations from -0.07 – 0.27
243 km/s (Line 4A) and from -0.2 – 0.29 km/s (Line 4B) (Suppl. Figs. 9,10).

244 **3. Results**

245 The final velocity models for Lines 4A and 4B have χ^2 values of 1.12 and 1.18,
246 respectively, with RMS misfits of 101 and 108 ms (Fig. 3). The upper sedimentary layer
247 on both lines has velocities ranging from 1.8 to 3.9 km/s and thicknesses ranging from
248 ~2.0 to ~5.5 km. On Line 4A, between 0 km and 100 km along-strike, there are
249 anomalously low velocities coincident to the OBS locations and a highly variable along-
250 strike structure which we believe is due to previously identified salt diapirs that were
251 observed on MCS reflection profiles (Dillon et al., 1982; Shillington et al., 2014; Tréhu et
252 al., 1989) (Fig. 3). The low-quality data on OBS A401-A406 and the low ray coverage
253 on the southern end of Line 4A are likely the result of these diapirs with very high
254 seismic velocities relative to the surrounding sediment (Figs. 2,3 Suppl. Figs. 4,5,6).
255 The lower sedimentary layers have velocities ranging from 2.9 to 5.9 km/s with
256 thicknesses ranging from ~2.7 to ~5.0 km (Fig. 3). The crustal layers have velocities
257 from 5.9 to 7.6 km/s with thicknesses from ~10.0 to ~13.0 km (Fig. 3). Velocities in the
258 crustal layers have more along-strike variability than the other layers, including two
259 anomalously low velocity regions between ~180 and ~210 km on Line 4A and between
260 ~105 and ~130 km on Line 4B where velocities just above the Moho only reach 6.9 to
261 7.0 km/s (Fig. 3). Within the upper mantle, velocities range from 7.9 to 8.1 km/s with
262 minimal along-strike variation. The layer boundary depths and seismic velocities
263 generally agree with previous tomography results in other parts of the margin (e.g.
264 Austin et al., 1990; Holbrook & Kelemen, 1993; LASE Study Group, 1986; Shuck et al.,
265 2019). At the intersection point with Line 1 and Line 2 from the ENAM-CSE, the Moho
266 on Lines 4A/4B is ~1-2 km deeper, which may represent slight differences in modeling

267 parameters (Shuck et al., 2019) or tradeoffs between lower crustal velocity and Moho
268 depth (Suppl. Figs. 9,10).



286 Figure 3) **Velocity modeling results.** Velocity models from Line 4A (A), Line 4B (B), and a combined
287 along-strike model (C). P-wave velocities in each model are contoured and correspond to the color bar.
288 Shaded and hatched region on Line 4A covers section of igneous crust with low ray coverage and
289 resolution due to overhead salt diapirs. The combined along-strike velocity model was made with the
portion of line 4A south of the intersection point and line 4B north of the intersection point.

290 To generate an along-strike view of the margin, we combined Lines 4A and 4B at
291 their intersection point near Cape Hatteras, NC (Figs. 1,3). At the intersection point,
292 velocities and boundary depths are in close agreement (Fig. 3). For this ~370-km-long
293 section of the margin, the most along-strike variability is contained within the crustal layer.
294 There is a slight thickening trend in the total crustal thickness and total sediment
295 thickness from south to north, but this appears predominately related to shallowing
296 bathymetry and the slight upslope orientation of Line 4B (Fig. 3, Suppl. Fig. 11). The
297 lower velocity regions in the lower crust on Lines 4A and 4B at distances of ~180 km to
298 ~210 km and ~245 km to ~285 km in the combined model are similar in size, but the
299 area on Line 4B has a slightly higher velocity (6.9 km/s vs 7.1 km/s) (Fig. 3).

300 **4. Discussion**

301 **4.1 Interpretation of the Velocity Model**

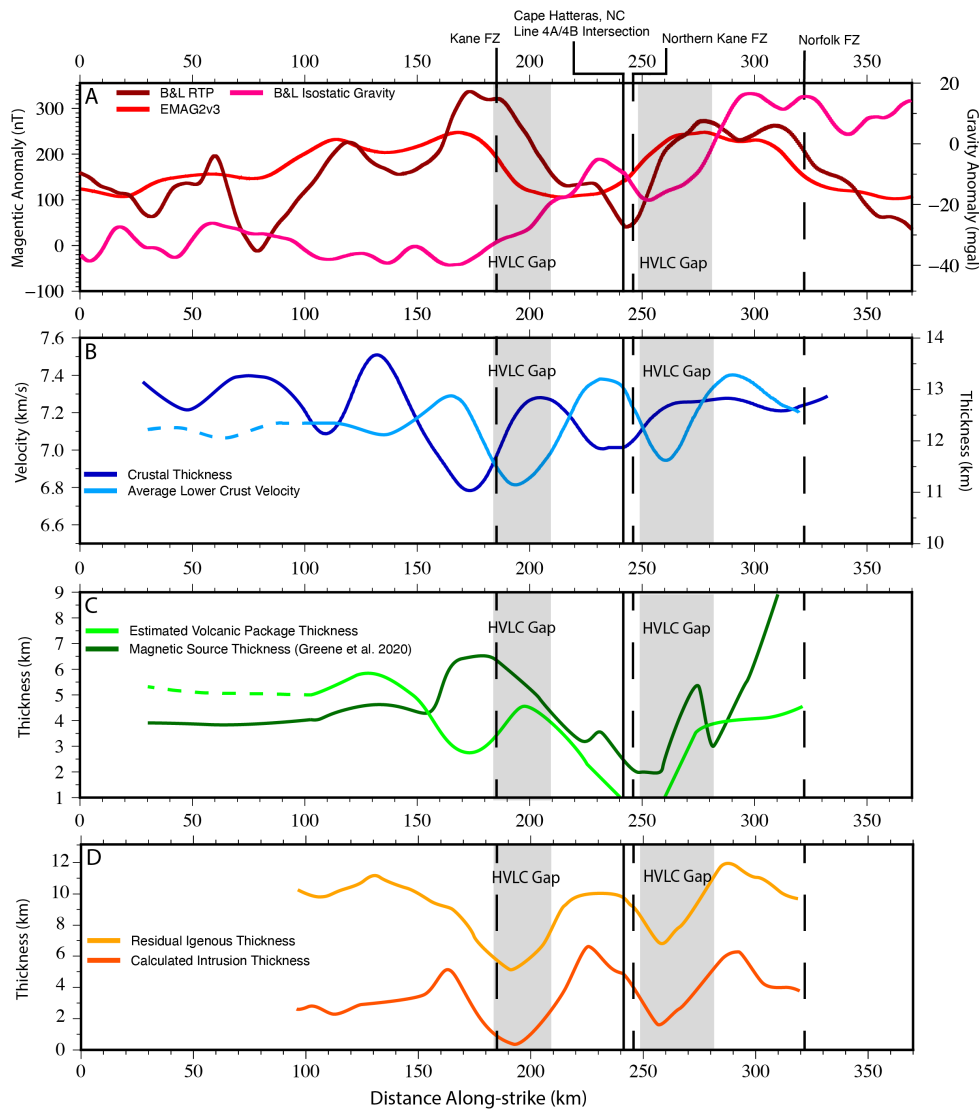
302 The new P-wave velocity models along Lines 4A and 4B show detailed along-
303 strike crustal structure beneath the ECMA for the first time, revealing significant
304 variations in lower crustal velocity. The upper crustal velocity structure is also laterally
305 heterogeneous, but changes in upper and lower crustal velocities are not tightly
306 correlated. Our results fill in gaps between previous, sparse margin perpendicular
307 observations and offer new insight into igneous addition during rifting and continental
308 breakup.

309 To interpret igneous materials beneath the ECMA, we used isovelocity contours
310 to approximate the areas of extrusive and intrusive addition. We use velocity contours
311 as our best approximation for because there were no reflections observed in the OBS
312 data that could delineate packages within the crust layer (Fig. 2) and initial processing

313 of coincident MCS reflection profiles from Lines 4A and 4B (Shillington et al., 2014)
314 showed little reflectivity within the basement that could be used to define boundaries. At
315 other volcanic margins, a lack of a mid-crustal reflection has been an indicator of
316 intrusion into the lower crust during rifting as opposed to underplating at the base of the
317 crust (Bécel et al., 2020; Eddy et al., 2014; Shuck et al., 2019; White et al., 2008).
318 Combined analysis of the wide-angle tomography results and MCS reflection profiles
319 from ENAM-CSE Lines 1 and 2 (Bécel et al., 2020; Shuck et al., 2019) show that the
320 upper portion of the SDR package in the MCS profile sits between the top of the crust
321 layer and the 6.5 km/s contour of the velocity model but these models did not image the
322 definitive base of the package. Along-strike variations in overburden can affect the
323 seismic velocities within the crust, we observe only small changes in sediment thickness
324 along-strike so this effect would be minimal (Fig. 3, Suppl. Fig. 11). Our uncertainty
325 analysis indicates that crustal velocities are well constrained with a depth uncertainty of
326 $\sim\pm 0.5$ km. Therefore, we use isovelocities to illuminate relative changes in both the
327 thickness of the volcanic layer and in the amount of synrift magmatic addition to the
328 lower crust in place of having a defined boundary.

329 Following previous investigators (e.g., Holbrook and Keleman, 1993; Shuck et
330 al., 2019), we used the 6.7 km/s contour to estimate the base of the extrusive (volcanic)
331 package and 7.2 km/s to estimate the top of the HVLC. With our isovelocity based
332 interpretation scheme, a volcanic package is present across both Lines 4A and 4B, with
333 a notable region between 210 km and 270 km along-strike where the 6.7 km/s contour
334 shallows to meet the top of the crust indicating significant thinning. HVLC is present on
335 both profiles except for two regions, from 170 – 220 km and 250 – 270 km in the along-

336 strike model, which have velocities less than ~ 7.2 km/s. We categorize these regions in
 337 the lower crust with reduced velocities as HVLC “gaps” because of the previously
 338 assumed prevalence of HVLC at the magma-rich ENAM (Fig. 3).



339
 340 Figure 4) **Along-strike analysis.** Vertical lines show the location of the line 4A/4B intersection point,
 341 Cape Hatteras, NC, and the Kane, Northern Kane, and Norfolk fracture zones. Vertical gray boxes represent
 342 location of the HVLC gaps. A) Geophysical anomalies coincident to our along-strike model including
 343 EMAG2V3, the RTP magnetic anomaly from Behn and Lin (2000), and the isostatic gravity anomaly from
 Behn and Lin (2000). B) Crustal thickness along-strike, calculated from the top of the crust layer to the
 Moho and the average lower crustal velocity. C) Estimated volcanic package thickness, calculated from the
 top of the crust to the 6.7 km/s velocity contour and the modeled magnetic source thickness from Greene
 et al. (2020). D) Calculated intrusion thickness into the lower crust based on the linear mixing calculation
 of Marzen et al. (2020) and the residual igneous thickness determined by adding the intrusion thickness
 to the volcanic thickness (light green line in C).

344 To further contextualize our results, we compare with regional potential fields
345 data (Fig. 4). The two-dimensional velocity models we present do not capture variable
346 3D structure that contributes to the potential fields, such that correlations between the
347 two may be imperfect, but some general correlations may be expected. Magnetic and
348 gravity anomalies along the ENAM show significant along-strike variation in amplitude
349 (Figs. 1,4) that should reflect changes in the magnetic source body and density
350 structure, respectively (e.g., Behn & Lin, 2000; Greene et al., 2020; Wyer & Watts,
351 2006). For the regions where we have reliable resolution, the reduced-to-pole (RTP)
352 magnetic anomaly appears to broadly be positively correlated with the estimated
353 volcanic thickness calculated from the top of the crustal layer to the 6.7 km/s contour
354 (Behn & Lin, 2000) (Fig. 4). The general correlation is consistent with the volcanic
355 package constituting the primary magnetic source (Austin et al., 1990; Davis et al.,
356 2018; Greene et al., 2017, 2020). In terms of gravity, the northern HVLC gap correlates
357 with a local minimum in the isostatic gravity anomaly but the southern HVLC gap does
358 not (Behn & Lin, 2000) (Fig. 4). The isostatic anomaly should be sensitive to variations
359 in density structure throughout the sediments, crust, and upper mantle, so the lack of
360 correlation with the southern HVLC gap could be due to its location within a larger trend
361 of decreasing gravity anomaly or 3D structures influencing the anomaly that that our 2D
362 lines cannot capture (Fig. 4).

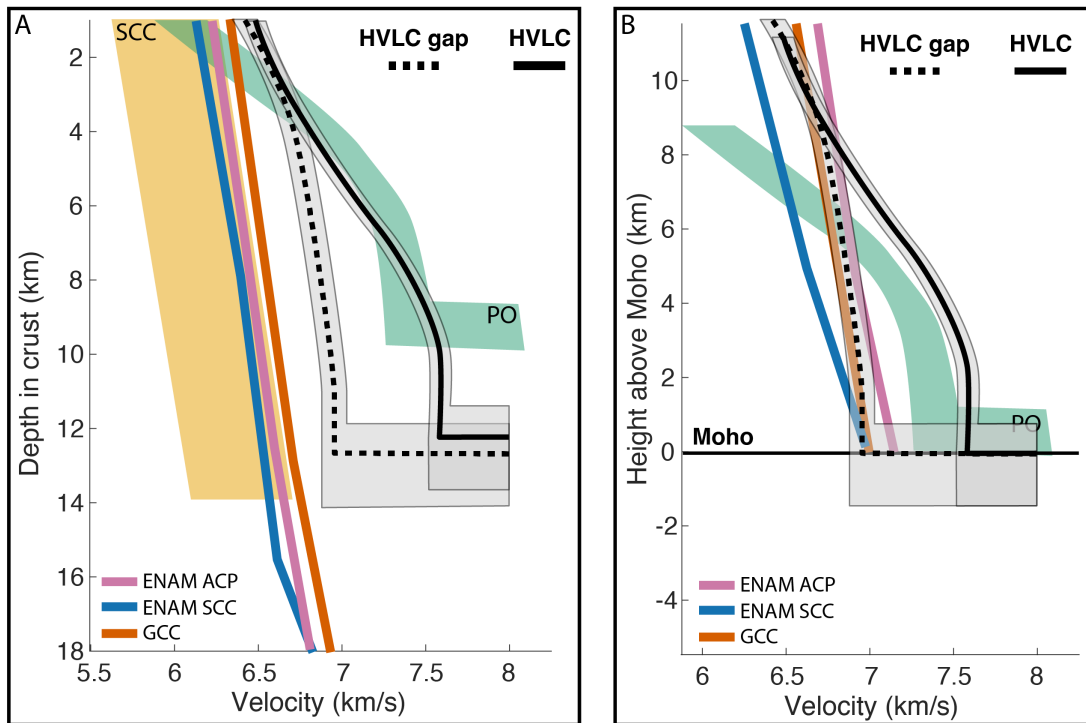
363 We also note that the estimated volcanic and HVLC thicknesses are not
364 correlated along-strike (Figs. 3,4). For example, south of the 4A/4B intersection a thick
365 section of volcanics overlies a section of crust without HVLC (Fig. 4). This observation is
366 surprising because both surface volcanics and the HVLC represent igneous addition to

367 the margin derived from the same mantle melt, so we might expect to find the thickest
368 volcanic sections above the thickest HVLC. Cape Hatteras, NC (coincident to the
369 intersection point) represents a change in margin orientation (Fig. 1), early seafloor
370 spreading regimes (Greene et al., 2017), and early rifting processes (Greene et al.,
371 2020), but it is difficult to know if those long wavelength variations would affect the
372 small-scale structure. While the upper and lower crust are both sourced from the same
373 mantle melt, and they are correlated on larger scales (>500 km), our results suggest
374 that the magmatic system is more complex at smaller scales.

375 **4.2 Origin of the Lower Crust Beneath the ECMA**

376 Previous studies that detected HVLC beneath the ECMA had considered it a
377 continuous, tabular shaped feature for the length of ENAM (e.g., Holbrook & Kelemen,
378 1993). Considering the distribution of HVLC in our along-strike view and in the models
379 from ENAM-CSE Lines 1 and 2 (Shuck et al., 2019), we suggest instead that the HVLC
380 may be more sporadically distributed along the margin. However, the origin of this
381 along-strike variability remains unclear. The crust beneath the ECMA is sandwiched
382 between the extended continental crust of the Atlantic coast plain (Luckie, 2017; Guo et
383 al., 2019) and continental shelf (Shuck et al., 2019) and anomalously thin, faulted, and
384 seismically fast proto-oceanic crust (Bécel et al., 2020; Shuck et al., 2019). Bécel et al.,
385 (2020) interpreted the crust beneath the ECMA as extrusive upper crust with
386 intermediate diking and lower crustal intrusion based on ENAM-CSE MCS profiles Lines
387 1 and 2 (Fig. 1), combined with collocated the wide-angle tomography (Shuck et al.,
388 2019). Many other passive margins show similar structure based on strike-
389 perpendicular seismic profiling (e.g Aslanian et al., 2021; Biari et al., 2017; Klingelhoefer

390 et al., 2009; Museur et al., 2021; White et al., 2008). Our observation that HVLC
 391 beneath the ENAM is discontinuous on ~30-km length scales, however, has not been
 392 observed at other margins with along-strike profiles (e.g., Aslanian et al., 2021;
 393 Contrucci et al., 2004; Klingelhofer et al., 2009; Reuber et al., 2016).



394 Figure 5) **One Dimensional Analysis.** Plots of the average 1D velocity profiles comparing the crust
 395 with HVLC and the crust with HVLC gaps to stretched continental crust (SCC) (Christensen and Mooney,
 396 1995), proto-oceanic crust (PO) (Shuck et al., 2019), continental crust from the Atlantic Coastal Plain
 397 (ENAM ACP) (Luckie 2017), continental crust from southern Georgia (GCC) (Marzen et al., 2020), and
 398 stretched continental crust from Line 1 and Line 2 landward of the ECMA (ENAM SCC) (Shuck et al.,
 2019). 1D velocity profiles are hung from their respective top of the crust (A) and are aligned at their
 respective Moho as determined by the authors (B). Gray boxes around the HVLC and HVLC gap profiles
 reflect estimated uncertainties in the model's crustal velocities and Moho depth.

399 To further investigate the nature of the heterogeneous lower crust beneath the
 400 ENAM, we calculated the average velocity-depth profile for crust with and without HVLC
 401 on Lines 4A and 4B. We compared the 1D profiles with the proto-oceanic crust from
 402 Lines 1 and 2 of the ENAM CSE and with a range of continental crust profiles from the
 403 Atlantic Coastal Plain, the ENAM continental shelf, the south Georgia Basin, and a

404 global baseline (Christensen & Mooney, 1995; Luckie, 2017; Marzen et al., 2020; Shuck
405 et al., 2019) (Fig. 5).

406 When hung from the top of the crust, the average one-dimensional velocity-depth
407 profile for sections with and without HVLC have nearly identical upper crustal velocities
408 that are close to the upper proto-oceanic crust, which would also have a volcanic origin
409 (Fig. 5A). Velocities near the top of the crust are slightly higher than the equivalent
410 proto-oceanic crust, but this difference could be due to the thicker sediment load
411 beneath the ECMA closing fractures and raising the velocity (Fig. 5A). At ~4 – 5 km
412 depth, the HVLC profile diverges, reaching ~7.5 km/s at the Moho as opposed to ~6.9
413 km/s for crust without HVLC (Fig. 5A). The velocity profile for the HVLC gaps is located
414 in between the proto-oceanic crust and the continental crustal profiles providing an
415 unclear origin (Fig. 5A).

416 To compare lower crustal structure more directly, we align the one-dimensional
417 velocity profiles at the Moho, as interpreted by the authors of each respective study
418 (Fig. 5B). In this view, the HVLC gap profile falls within the range of lower continental
419 crust from eastern North America (Luckie, 2017; Marzen et al., 2020; Shuck et al.,
420 2019), suggesting that these sections represent lower continental crust that was not
421 intruded during rifting (Fig. 5B). Studies at other Atlantic passive margins have found
422 that the middle to lower continental crust may persist through extension becoming the
423 base of transitional margin crust (e.g. Aslanian et al., 2021; Biari et al., 2017; Contrucci
424 et al., 2004; Klingelhoefer et al., 2009). Based on this analysis, we suggest that the
425 along-strike variation in the lower crust velocity structure beneath the ECMA reflects

426 alternating sections of extensive and limited intrusion into lower continental crust (Fig.
427 6).

428 **4.3 Igneous Addition During Continental Breakup**

429 Volcanic margins are defined by a significant volume of igneous addition, and
430 several previous studies have attempted to calculate the ENAM's total igneous volume.
431 We first use our interpreted velocity models to approximate the proportion of extrusive
432 and intrusive magmatism at the ENAM as this ratio is frequently used to estimate the
433 total volume for the margin. A recent global analysis of volcanic rifted margins found an
434 average thickness ratio of 1:3 between SDRs and HVLC, providing a baseline value for
435 the ratio of extrusive to intrusive rocks (Gallahue et al., 2020). Observations in both
436 active and failed rifts (e.g., the Midcontinent Rift (Elling et al., 2020), the Afar Rift
437 (Bastow & Keir, 2011), and the Main Ethiopian Rift (Keranen et al., 2004)) and at
438 volcanic passive margins (e.g., offshore Norway (Faleide et al., 2008), South America
439 (Becker et al., 2014), and southwest Africa (Koopmann et al., 2014)) indicate that
440 SDR:HVLC thickness ratios may vary along-strike, but there has not been a detailed
441 along-strike analysis of the ratio at the ENAM.

442 By comparing our isovelocity derived thicknesses (e.g., Fig. 4), we find that the
443 ratio between the volcanics and the HVLC in this part of the ENAM is $1:2 \pm 0.25$ on
444 average. However, this estimate assumes that the entire lower crust is fully formed from
445 igneous addition, not heavily intruded continental crust. To refine our estimate, we
446 calculated the along-strike igneous intrusion thickness into the crust using a linear
447 mixing equation following the methods of White et al. (2008) and Marzen et al. (2020)
448 (Fig. 4). Assuming a background lower crustal velocity of 6.8 km/s and a mafic intrusion

449 velocity of 7.5 km/s, the intrusion thickness ranges from ~0.5 km to ~6.5 km with local
450 minimums coincident to the HVLC gaps (Fig. 4). Adding the estimated volcanic package
451 thickness to the calculated intrusion thickness represents the total igneous thickness
452 along-strike, which varies more significantly than the overall crustal thickness (Fig. 4).

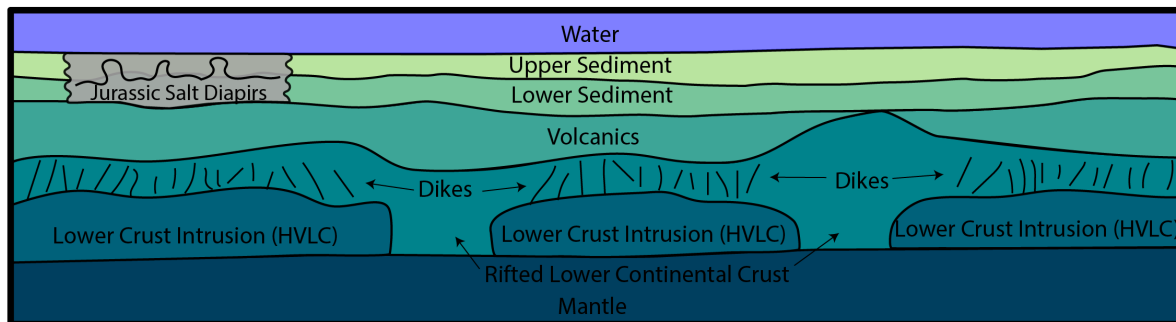
453 The updated intrusion thickness reduces the extrusive:intrusive ratio to
454 1:1.25±.25 which is similar to the ratio determined by White et al. (2008) in the North
455 Atlantic. Without a modeled reflector separating the volcanics and HVLC, our ratio is
456 dependent on the specific isovelocity chosen as the proxy boundary. A different chosen
457 velocity would result in a slightly different ratio, but our results indicate that the ratio is
458 generally lower than previous estimates from ENAM and the recent global compilation
459 from Gallahue et al. (2020).

460 Holbrook & Kelemen (1993) calculated a maximum igneous volume of $\sim 3.2 \times 10^6$
461 km^3 using the cross-sectional area of imaged SDRs and HVLC on transects BA-6 and
462 EDGE 801 multiplied by the margin length (Fig. 1). Greene et al. (2020) modeled the
463 margin-wide ECMA magnetic source and used the SDR:HVLC relation of Gallahue et
464 al. (2020) (SDR:HVLC = 1:3) to estimate a total volume of $\sim 1.6 \times 10^6 \text{ km}^3$, a 50%
465 reduction. While the Greene et al. (2020) estimate accounts for variability along the
466 margin, it relies on a global relationship that may not apply to the ENAM. Using our new
467 calculated ratio along the entire margin, the Greene et al. (2020) estimate would reduce
468 by ~48% to $8.39 \pm 0.93 \times 10^5 \text{ km}^3$. In addition to the updated ratio, the observed
469 discontinuities in HVLC along the rest of the margin would further reduce the volume by
470 a potentially significant amount. However, it remains unclear how prevalent the HVLC
471 discontinuities are along the ENAM. These volume estimates are not definitive, but add

472 to a growing body of evidence that magmatism during the formation of the ENAM was
473 less voluminous and more irregularly distributed than previously thought (e.g., Bécél et
474 al., 2020; Greene et al., 2020; Marzen et al., 2020; Shuck et al., 2019)

475 4.4 Magmatic Segmentation During Early Rifting

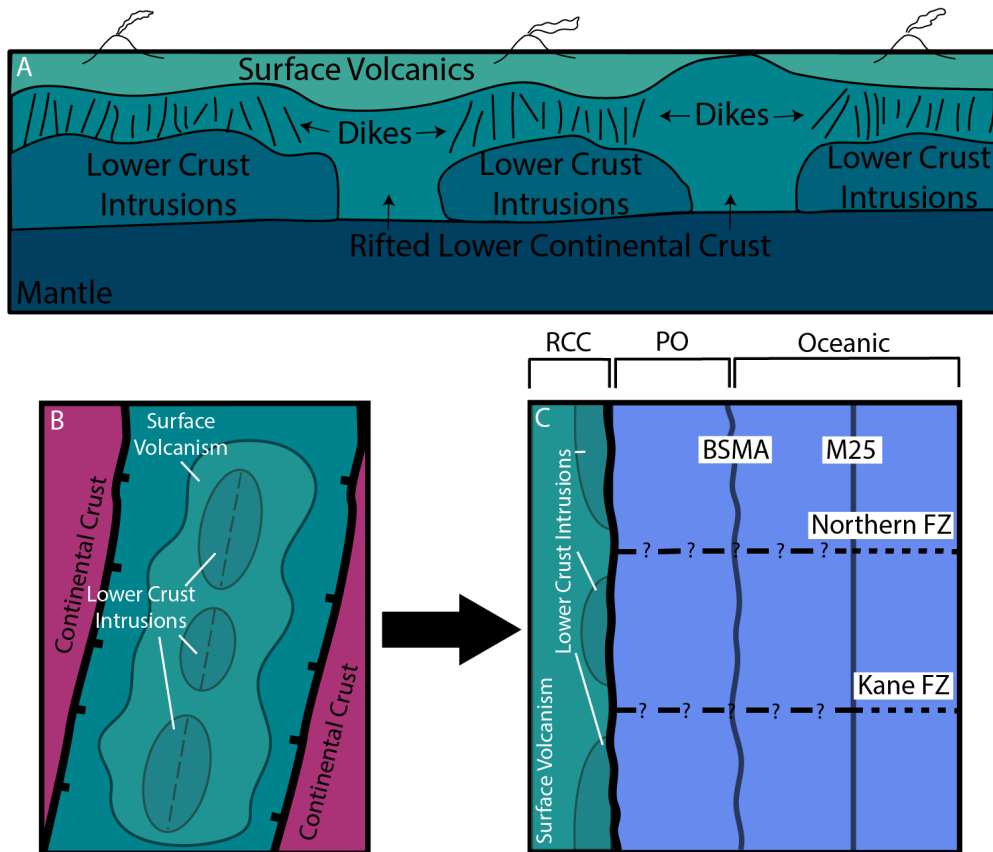
476 Our interpretation that there are variable degrees of intrusion beneath the ECMA
477 provides evidence for along-strike magmatic segmentation during the rifting process
478 (Figs. 6,7). We suggest that there were discrete sites of magmatic intrusion in the
479 continental rift that correlate to the areas with HVLC while gaps between the magmatic
480 centers remained unintruded (Fig. 7). Extensive volcanism covered the rift surface,
481 sometimes flowing away from the magmatic centers to cover the unintruded crust,
482 which is imaged now as the volcanic upper crust (Figs. 3,6,7).



483 Figure 6) **Interpretation of the Crust.** Conceptual model of the along-strike geology beneath the
484 ECMA with interpreted velocity models structures. The along-strike velocity model's crust layer is
485 comprised of a volcanic package and intrusions into the lower crust (HVLC) with diking in between
486 following interpretation by Bécél et al., (2020). HVLC gaps in the velocity model are interpreted as
487 rifted lower continental crust with no intrusion.

488 Magmatic segmentation has been observed in the active Main Ethiopian Rift and
489 in the Afar Rift where significant volcanism and crustal intrusion occur in ~30 km to
490 ~100 km long and ~20 km wide segments near the rift axis (Ebinger & Casey, 2001;
Hammond et al., 2011; Hayward & Ebinger, 1996; Keranen et al., 2004). Velocities at

491 the ENAM are faster than in the East African Rift, perhaps reflective of more mature
 492 crust with more significant magmatism at the ENAM (Hammond et al., 2011; Keranen et
 493 al., 2004). Segmentation during early-stage rifting may also manifest by border faults,
 494 some of which alternate in polarity, such as at the Midcontinent Rift or in the Malawi Rift
 495 (Dickas et al., 1997; Scholz et al., 2020). Border-fault-defined segmentation may be
 496 abandoned when magmatism and magmatic volatiles become involved and/or
 497 extension migrates to other fault systems (e.g. Ebinger & Casey, 2001; Muirhead et al.,
 498 2016).



499
 500 **Figure 7) Conceptual segmentation model.** A) A hypothetical cross section beneath the active
 501 continental rift with developed magmatic segmentation (discontinuous lower crust intrusions) and
 502 surface volcanics. B) Map view of the magmatic segmentation in the continental rift. C) The continental
 rift evolved into the Mid-Atlantic Ridge with successful breakup, and the correlation of fracture zones
 to the discontinuous HVLC gaps suggest a rift to ridge connection, but the fracture zones cannot be
 traced directly to the ECMA. BSMA is Blake Spur Magnetic Anomaly. RCC is rifted continental crust. PO
 is proto-oceanic crust defined by Shuck et al., (2019).

503

504 The cause of magmatic segmentation at the ENAM is unclear. In some locations
505 segmentation may be driven by pre-existing structures that serve as zones of
506 weakness, facilitating extension and magmatism (Frizon de Lamotte et al., 2015). The
507 ENAM has experienced multiple Wilson cycles and exhibits evidence pointing to
508 structural controls on segmentation (Thomas, 2006). However, in our study area, the
509 segmentation we observe does not appear to correlate with pre-existing structures,
510 including a suture zone and onshore basement arches (Figs. 1,3). Magmatic
511 segmentation may also be driven by small scale convection in the upper mantle,
512 providing a source of heat to weaken the lithosphere and a source of melt for
513 magmatism (Gac & Geoffroy, 2009; Geoffroy et al., 2001). It is unclear if this would
514 allow for the small-scale gaps we observe in the lower crust, or if it is more related to
515 longer wavelength segmentation.

516 Notably, the observed along-strike variations in lower crustal structure are
517 coincident with the westward extent of extrapolated fracture zones from the Mid-Atlantic
518 Ridge, which indicates a possible connection between rift and ridge segmentation (Behn
519 and Lin, 2000; Greene et al., 2017) (Figs. 3,4,7). Petrological-thermomechanical
520 modeling from some passive margins and active rifts suggests that magmatism drives
521 segmentation and that the rift segments can evolve directly into spreading segment, but
522 it is unclear if this process occurred at the ENAM or the spatial correlation is a
523 coincidence (Gerya, 2013; Illsley-Kemp et al., 2018; Taylor et al., 2009). The lack of
524 fracture zone identification between M25 and the ECMA, excluding the faint lineation
525 offsets observed by Greene et al. (2017), and the lack of correlated structures at the

526 BSMA (Shuck et al., 2019), make it difficult to draw a definitive conclusion (Figs. 1,7).
527 Further imaging of the ENAM, or other passive margins, may illuminate additional
528 along-strike variability in crustal structure and could provide stronger evidence of the rift
529 to ridge connection which is crucial for our continued understanding of continental
530 breakup and mid-ocean ridge formation.

531 **5. Conclusions**

532 1) New tomographically-derived seismic velocity models along the ECMA show that
533 crustal structure is significantly more variable along-strike than previously thought, with
534 most variability located in the lower crust. Two large “gaps” in HVLC are present in the
535 lower crust where velocities reach ~6.9 - 7.0 km/s above the Moho compared to ~7.3 -
536 7.5 km/s within the HVLC.

537

538 2) The average one dimensional velocity structure of the HVLC “gaps” match rifted
539 lower continental crust in velocity-depth space, indicating that these areas were not
540 intruded or were minimally intruded during breakup. Therefore, the along-strike crustal
541 structure beneath the ECMA consists of discrete regions of intrusion (the HVLC) and
542 regions with very limited intrusion (the HVLC gaps) covered by a volcanic layer.

543

544 3) The average lower crustal velocity and the estimated extrusive igneous thickness are
545 not correlated, indicating extensive surface volcanism regardless of lower crustal
546 intrusions. We estimate that the igneous thickness along-strike, calculated with linear
547 mixing, is ~2.5 km to ~6.0 km less than the than total crustal thickness.

548

549 4) The ratio of extrusive to intrusive thicknesses in the igneous crust beneath the ECMA
550 is less than previously defined by global studies and strike perpendicular profiles. Our
551 estimated ratio of 1 to $1.25 \pm .25$ lowers recent estimates of the ENAM's total volume by
552 ~48%.

553

554 5) The along-strike crustal variability is on similar scales to observations made at active
555 and failed continental rifts, implying that our observations reflect magmatic
556 segmentation during early rifting. The magmatic segmentation approximately aligns with
557 Mid-Atlantic Ridge fracture zones suggesting that segmentation of the rift could be
558 related to segmentation of the ridge, but further along-strike imaging of the ENAM is
559 needed to establish a definitive relationship.

560

561 **DATA and ACKNOWLEDGEMENTS**

562 The ENAM-CSE study area includes [traditional lands and waters](#) of [many Indigenous](#)
563 [peoples](#), including the Lumbee, Skaruhreh/Tuscarora, Hatteras, Roanoke and
564 Chesapeake territories. The data used in this analysis is freely available at the Marine
565 Geoscience Data System Portal under expedition code EN546: [https://www.marine-](https://www.marine-geo.org/tools/search/Files.php?data_set_uid=27784)
566 [geo.org/tools/search/Files.php?data_set_uid=27784](https://www.marine-geo.org/tools/search/Files.php?data_set_uid=27784) (doi: [10.1594/IEDA/500017](https://doi.org/10.1594/IEDA/500017)). We
567 thank the principal investigators of the ENAM-CSE, the captains and crews of the R/V
568 *Langseth* and R/V *Endeavor*, and the many technicians, students and scientists that
569 contributed to the community dataset acquisition. Masako Tominaga, John Greene, and
570 Brandon Shuck provided constructive comments and discussion during preparation of

571 this manuscript. This work was supported by NSF awards OCE-1654804 to
572 Worthington, OCE-1654781 to Magnani and OCE-1654629 to Shillington.

573

574 **References**

575

576 Alsop, L. E., & Talwani, M. (1984). The east coast magnetic anomaly. *Science*,
577 226(4679), 1189–1191.

578 Aslanian, D., Gallais, F., Afilhado, A., Schnurle, P., Moulin, M., Evain, M., et al. (2021).
579 Deep structure of the Pará-Maranhão/Barreirinhas passive margin in the equatorial
580 Atlantic (NE Brazil). *Journal of South American Earth Sciences*, 110(December
581 2020), 103322. <https://doi.org/10.1016/j.jsames.2021.103322>

582 Austin, J. A., Stoffa, P. L., Phillips, J. D., Oh, J., Sawyer, D. S., Purdy, G. M., et al.
583 (1990). Crustal structure of the Southeast Georgia embayment-Carolina trough:
584 Preliminary results of a composite seismic image of a continental suture (?) and a
585 volcanic passive margin. *Geology*, 18(10), 1023–1027.

586 Bastow, I. D., & Keir, D. (2011). The protracted development of the continent–ocean
587 transition in Afar. *Nature Geoscience*, 4(4), 248–250.

588 Bécel, A., Davis, J. K., Gibson, J. C., Shuck, B. D., Van Avendonk, H. J. A., & Gibson, J.
589 C. (2020). Evidence for a Prolonged Continental Breakup resulting from Slow
590 Extension Rates at the Eastern North American Volcanic Rifted Margin. *Journal of*
591 *Geophysical Research: Solid Earth*, e2020JB020093.
592 <https://doi.org/10.1029/2020JB020093>

593 Becker, K., Franke, D., Trumbull, R., Schnabel, M., Heyde, I., Schreckenberger, B., et
594 al. (2014). Asymmetry of high-velocity lower crust on the South Atlantic rifted
595 margins and implications for the interplay of magmatism and tectonics in
596 continental breakup. *Solid Earth*, 5(2), 1011–1026.

597 Behn, M. D., & Lin, J. (2000). Segmentation in gravity and magnetic anomalies along
598 the US East Coast passive margin: Implications for incipient structure of the
599 oceanic lithosphere. *Journal of Geophysical Research: Solid Earth*, 105(B11),
600 25769–25790.

601 Bialas, R. W., Buck, W. R., & Qin, R. (2010). How much magma is required to rift a
602 continent? *Earth and Planetary Science Letters*, 292(1–2), 68–78.

603 Biari, Y., Klingelhoefer, F., Sahabi, M., Funck, T., Benabdellouahed, M., Schnabel, M.,
604 et al. (2017). Opening of the central Atlantic Ocean: implications for geometric
605 rifting and asymmetric initial seafloor spreading after continental breakup.
606 *Tectonics*, 36(6), 1129–1150.

607 Buck, R. (2006). The role of magma in the development of the Afro-Arabian Rift System.
608 *Geological Society, London, Special Publications*, 43–54.
609 <https://doi.org/10.1144/GSL.SP.2006.259.01.05>

610 Christensen, N. I., & Mooney, W. D. (1995). Seismic velocity structure and composition
611 of the continental crust: A global view. *Journal of Geophysical Research: Solid*
612 *Earth*, 100(B6), 9761–9788.

613 Contrucci, I., Matias, L., Moulin, M., Géli, L., Klingelhoefer, F., Nouzé, H., et al. (2004).

614 Deep structure of the West African continental margin (Congo, Zaire, Angola),
615 between 5 S and 8 S, from reflection/refraction seismics and gravity data.
616 *Geophysical Journal International*, 158(2), 529–553.

617 Davis, J. K., Bécel, A., & Buck, W. R. (2018). Estimating emplacement rates for
618 seaward-dipping reflectors associated with the US East Coast Magnetic Anomaly.
619 *Geophysical Journal International*, 215(3), 1594–1603.

620 Dickas, A. B., Mudrey, M. G., Ojakangas, R. W., & Green, J. C. (1997). Segmented
621 structure of the middle Proterozoic Midcontinent rift system, North America.
622 *SPECIAL PAPERS-GEOLOGICAL SOCIETY OF AMERICA*, 37–46.

623 Dillon, W. P., Popenoe, P., Grow, J. A., Klitgord, K. D., Swift, B. A., Paull, C. K., &
624 Cashman, K. V. (1982). Growth Faulting and Salt Diapirism: Their Relationship and
625 Control in the Carolina Trough, Eastern North America: Rifted Margins: Field
626 Investigations of Margin Structure and Stratigraphy.

627 Ebinger, C., & Casey, M. (2001). Continental breakup in magmatic provinces: An
628 Ethiopian example. *Geology*, 29(6), 527–530.

629 Eddy, D. R., Van Avendonk, H. J. A., Christeson, G. L., Norton, I. O., Karner, G. D.,
630 Johnson, C. A., & Snedden, J. W. (2014). Deep crustal structure of the
631 northeastern Gulf of Mexico: Implications for rift evolution and seafloor spreading.
632 *Journal of Geophysical Research: Solid Earth*, 119(9), 6802–6822.

633 Elling, R. P., Stein, S., Stein, C. A., & Keller, G. R. (2020). Tectonic implications of the
634 gravity signatures of the Midcontinent Rift and Grenville Front. *Tectonophysics*,
635 778, 228369.

636 Faleide, J. I., Tsikalas, F., Breivik, A. J., Mjelde, R., Ritzmann, O., Engen, O., et al.
637 (2008). Structure and evolution of the continental margin off Norway and the
638 Barents Sea. *Episodes*, 31(1), 82–91.

639 Franke, D., Neben, S., Ladage, S., Schreckenberger, B., & Hinz, K. (2007). Margin
640 segmentation and volcano-tectonic architecture along the volcanic margin off
641 Argentina/Uruguay, South Atlantic. *Marine Geology*, 244(1–4), 46–67.

642 Frizon de Lamotte, D., Fourdan, B., Leleu, S., Leparmentier, F., & de Clarens, P.
643 (2015). Style of rifting and the stages of Pangea breakup. *Tectonics*, 34(5), 1009–
644 1029.

645 Gac, S., & Geoffroy, L. (2009). 3D Thermo-mechanical modelling of a stretched
646 continental lithosphere containing localized low-viscosity anomalies (the soft-point
647 theory of plate break-up). *Tectonophysics*, 468(1–4), 158–168.

648 Gallahue, M. M., Stein, S., Stein, C. A., Jurdy, D., Barklage, M., & Rooney, T. O. (2020).
649 A compilation of igneous rock volumes at volcanic passive continental margins from
650 interpreted seismic profiles. *Marine and Petroleum Geology*, 122(August), 104635.
651 <https://doi.org/10.1016/j.marpetgeo.2020.104635>

652 Geoffroy, L., Callot, J., Scaillet, S., Skuce, A., Gélard, J. P., Ravilly, M., et al. (2001).
653 Southeast Baffin volcanic margin and the North American-Greenland plate
654 separation. *Tectonics*, 20(4), 566–584.

655 Geoffroy, L., Burov, E. B., & Werner, P. (2015). Volcanic passive margins: another way
656 to break up continents. *Scientific Reports*, 5(1), 1–12.

657 Gerya, T. V. (2013). Initiation of transform faults at rifted continental margins: 3D
658 petrological-thermomechanical modeling and comparison to the Woodlark Basin.
659 *Petrology*, 21(6), 550–560.

660 Gerya, Taras V. (2013). Three-dimensional thermomechanical modeling of oceanic
661 spreading initiation and evolution. *Physics of the Earth and Planetary Interiors*, 214,
662 35–52.

663 Greene, J. A., Tominaga, M., Miller, N. C., Hutchinson, D. R., & Karl, M. R. (2017).
664 Refining the Formation and Early Evolution of the Eastern North American Margin:
665 New Insights From Multiscale Magnetic Anomaly Analyses. *Journal of Geophysical*
666 *Research: Solid Earth*. <https://doi.org/10.1002/2017JB014308>

667 Greene, J. A., Tominaga, M., & Miller, N. C. (2020). Along-Margin Variations in Breakup
668 Volcanism at the Eastern North American Margin. *Journal of Geophysical*
669 *Research: Solid Earth*, e2020JB020040. <https://doi.org/10.1029/2020JB020040>

670 Hammond, J. O. S., Kendall, J., Stuart, G. W., Keir, D., Ebinger, C., Ayele, A., &
671 Belachew, M. (2011). The nature of the crust beneath the Afar triple junction:
672 Evidence from receiver functions. *Geochemistry, Geophysics, Geosystems*, 12(12).
673 <https://doi.org/10.1029/2011GC003738>

674 Hayward, N. J., & Ebinger, C. J. (1996). Variations in the along-axis segmentation of the
675 Afar Rift system. *Tectonics*, 15(2), 244–257.

676 Holbrook, & Kelemen, P. B. (1993). Large igneous province on the US Atlantic margin
677 and implications for magmatism during continental breakup. *Nature*, 364(6436),
678 433.

679 Illsley-Kemp, F., Bull, J. M., Keir, D., Gerya, T., Pagli, C., Gernon, T., et al. (2018).
680 Initiation of a proto-transform fault prior to seafloor spreading. *Geochemistry,*
681 *Geophysics, Geosystems*, 19(12), 4744–4756.
682 <https://doi.org/10.1029/2018GC007947>

683 Keranen, K., Klemperer, S. L., Gloaguen, R., & Group, E. W. (2004). Three-dimensional
684 seismic imaging of a protoridge axis in the Main Ethiopian rift. *Geology*, 32(11),
685 949–952.

686 Klingelhoefer, F., Labails, C., Cosquer, E., Rouzo, S., Geli, L., Aslanian, D., et al.
687 (2009). Crustal structure of the SW-Moroccan margin from wide-angle and
688 reflection seismic data (the DAKHLA experiment) Part A: Wide-angle seismic
689 models. *Tectonophysics*, 468(1–4), 63–82.
690 <https://doi.org/10.1016/j.tecto.2008.07.022>

691 Klitgord, K. D., & Schouten, H. (1986). Plate kinematics of the central Atlantic. *The*
692 *Western North Atlantic Region*.

693 Koopmann, H., Franke, D., Schreckenberger, B., Schulz, H., Hartwig, A., Stollhofen, H.,
694 & di Primio, R. (2014). Segmentation and volcano-tectonic characteristics along the
695 SW African continental margin, South Atlantic, as derived from multichannel
696 seismic and potential field data. *Marine and Petroleum Geology*, 50, 22–39.

697 Korenaga, J., Kelemen, P. B., & Holbrook, W. S. (2002). Methods for resolving the
698 origin of large igneous provinces from crustal seismology. *Journal of Geophysical*
699 *Research: Solid Earth*, 107(B9), ECV-1.

700 LASE Study Group, L. S. (1986). Deep structure of the US East Coast passive margin
701 from large aperture seismic experiments (LASE). *Marine and Petroleum Geology*,
702 3(3), 234–242.

703 Luckie, T. W. (2017). Insights on magmatic addition beneath the mid-Atlantic Coastal
704 Plain from crustal seismic refraction data.

705 Lynner, C., Van Avendonk, H. J. A., Bécél, A., Christeson, G. L., Dugan, B., Gaherty, J.

706 B., et al. (2019). The Eastern North American Margin Community Seismic
707 Experiment: An Amphibious Active-and Passive-Source Dataset. *Seismological*
708 *Research Letters*.

709 Marzen, R. E., Shillington, D. J., Lizarralde, D., Knapp, J. H., Heffner, D. M., Davis, J.
710 K., & Harder, S. H. (2020). Limited and localized magmatism in the Central Atlantic
711 Magmatic Province. *Nature Communications*, *11*(1), 1–8.
712 <https://doi.org/10.1038/s41467-020-17193-6>

713 Marzoli, A., Callegaro, S., Dal Corso, J., Davies, J. H. F. L., Chiaradia, M., Youbi, N., et
714 al. (2018). The Central Atlantic magmatic province (CAMP): a review. In *The Late*
715 *Triassic World* (pp. 91–125). Springer. <https://doi.org/10.1007/978-3-319-68009-5>

716 Muirhead, J. D., Kattenhorn, S. A., Lee, H., Mana, S., Turrin, B. D., Fischer, T. P., et al.
717 (2016). Evolution of upper crustal faulting assisted by magmatic volatile release
718 during early-stage continental rift development in the East African Rift. *Geosphere*,
719 *12*(6), 1670–1700.

720 Museur, T., Graindorge, D., Klingelhoefer, F., Roest, W. R., Basile, C., Loncke, L., &
721 Sapin, F. (2021). Deep structure of the Demerara Plateau: From a volcanic margin
722 to a Transform Marginal Plateau. *Tectonophysics*, *803*, 228645.

723 Reuber, K. R., Pindell, J., & Horn, B. W. (2016). Demerara Rise, offshore Suriname:
724 Magma-rich segment of the Central Atlantic Ocean, and conjugate to the Bahamas
725 hot spot. *Interpretation*, *4*(2), T141–T155.

726 Scholz, C. A., Shillington, D. J., Wright, L. J. M., Accardo, N., Gaherty, J. B., &
727 Chindandali, P. (2020). Intrarift fault fabric, segmentation, and basin evolution of
728 the Lake Malawi (Nyasa) Rift, East Africa. *Geosphere*, *16*(5), 1293–1311.

729 Schouten, H., Klitgord, K. D., & Whitehead, J. A. (1985). Segmentation of mid-ocean
730 ridges. *Nature*, *317*(6034), 225–229.

731 Shillington, D., Bécel, A., Hornbach, M., Lizarralde, D., Magnani, M. B., Van Avendonk,
732 H., et al. (2014). Processed multichannel seismic data off North Carolina and
733 Virginia, acquired during R/V Marcus G. Langseth expedition MGL1408 (2014) as
734 part of the Eastern North America Community Seismic Experiment (ENAM).
735 Interdisciplinary Earth Data Alliance (IEDA), doi.

736 Shuck, B., Van Avendonk, H. J. A., & Bécel, A. (2019). The role of mantle melts in the
737 transition from rifting to seafloor spreading offshore eastern North America. *Earth*
738 *and Planetary Science Letters*, *525*, 115756.

739 Taylor, B., Goodliffe, A., Martinez, F., & Hey, R. (1995). Continental rifting and initial
740 sea-floor spreading in the Woodlark Basin. *Nature*, *374*(6522), 534–537.

741 Taylor, B., Goodliffe, A., & Martinez, F. (2009). Initiation of transform faults at rifted
742 continental margins. *Comptes Rendus Geoscience*, *341*(5), 428–438.

743 Thomas, W. A. (2006). Tectonic inheritance at a continental margin. *GSA Today*, *16*(2),
744 4–11.

745 Thybo, H., & Nielsen, C. A. (2009). Magma-compensated crustal thinning in continental
746 rift zones. *Nature*, *457*(7231), 873–876.

747 Thybo, Hans, & Artemieva, I. M. (2013). Moho and magmatic underplating in continental
748 lithosphere. *Tectonophysics*, *609*, 605–619.

749 Tréhu, A. M., Ballard, A., Dorman, L. M., Gettrust, J. F., Klitgord, K. D., & Schreiner, A.
750 (1989). Structure of the lower crust beneath the Carolina Trough, US Atlantic
751 continental margin. *Journal of Geophysical Research: Solid Earth*, *94*(B8), 10585–

752 10600.
753 Van Avendonk, H., Shillington, D. J., Holbrook, W. S., & Hornbach, M. J. (2004).
754 Inferring crustal structure in the Aleutian island arc from a sparse wide-angle
755 seismic data set. *Geochemistry, Geophysics, Geosystems*, 5(8).
756 Van Avendonk, H., (2015). Ocean bottom seismometer data, updated with relocated
757 instrument coordinates, off North Carolina and Virginia, acquired during R/V
758 Endeavor expedition EN546 (2014) as part of the Eastern North America
759 Community Seismic Experiment (ENAM). IEDA. doi:[10.1594/IEDA/500017](https://doi.org/10.1594/IEDA/500017)
760 White, R. S., Smith, L. K., Roberts, A. W., Christie, P. A. F., & Kusznir, N. J. (2008).
761 Lower-crustal intrusion on the North Atlantic continental margin. *Nature*, 452(7186),
762 460–464.
763 Wyer, P., & Watts, A. B. (2006). Gravity anomalies and segmentation at the East Coast,
764 USA continental margin. *Geophysical Journal International*, 166(3), 1015–1038.
765

1 **Discontinuous Igneous Addition along the Eastern North American**
2 **Margin beneath the East Coast Magnetic Anomaly**

3 **Collin C. Brandl¹, Lindsay Lowe Worthington¹, Maria Beatrice Magnani²,**
4 **Donna J. Shillington³, Thomas W. Luckie⁴**

5
6 ¹ Department of Earth and Planetary Sciences, The University of New Mexico,
7 Albuquerque, New Mexico 87131, USA

8 ² Department of Earth Sciences, Southern Methodist University, Dallas, Texas 75275,
9 USA

10 ³ School of Earth and Sustainability, Northern Arizona University, Flagstaff, Arizona
11 86011, USA

12 ⁴ Department of Earth Sciences, University of Southern California, Los Angeles,
13 California 90089, USA

14 Corresponding author: Collin Brandl (cbrandl@unm.edu)

15 Key Points:

- 16 - High velocity lower crust beneath the East Coast Magnetic Anomaly is
17 discontinuous and represents magmatic segmentation during rifting
- 18 - The extrusive:intrusive ratio at the ENAM is lower than the global average
19 resulting in a significantly reduced total igneous volume
- 20 - The HVLC discontinuities are coincident to Mid-Atlantic Ridge fracture zones,
21 potentially indicating a rift to ridge connection

22

23 **Abstract**

24 Detailed models of crustal structure at volcanic passive margins offer insight into the
25 role of magmatism and distribution of igneous addition during continental rifting. The
26 Eastern North American Margin (ENAM) is a volcanic passive margin that formed during
27 the breakup of Pangea ~200 Myr ago. The offshore, margin-parallel East Coast
28 Magnetic Anomaly (ECMA) is thought to mark the locus of synrift magmatism. Previous
29 widely spaced margin-perpendicular studies seismically imaged igneous addition as
30 seaward dipping reflectors (SDRs) and high velocity lower crust (HVLC; >7.2 km/s)
31 beneath the ECMA. Along-strike imaging is necessary to more accurately determine the
32 distribution and volume of igneous addition during continental breakup. We use wide-
33 angle, marine active-source seismic data from the 2014-2015 ENAM Community
34 Seismic Experiment to determine crustal structure beneath a ~370-km-long section of
35 the ECMA. P-wave velocity models based on data from short-period ocean bottom
36 seismometers reveal a ~21-km-thick crust with laterally variable lower crust velocities
37 ranging from 6.9 to 7.5 km/s. Sections with HVLC alternate with two ~30-km-wide areas
38 where the velocities do not exceed 7.0 km/s. This variable structure indicates that HVLC
39 is discontinuous along the margin. Velocity-thickness analysis indicates that the HVLC
40 discontinuity is the result of variable intrusion along-strike. Our results suggest that
41 magmatism during early rifting was segmented and was lower in volume than previously
42 thought. The HVLC discontinuities roughly align with locations of Mid-Atlantic Ridge
43 fracture zones, which may indicate that early rift segmentation influenced later
44 segmentation of the Mid-Atlantic Ridge.

45 **Plain Language Summary**

46 The East Coast of the United States is a passive margin that formed during continental
47 breakup of Pangea, the most recent supercontinent. Although passive margins are
48 generally not locales of active faulting and magmatism, by investigating their current
49 structure, we gain insight into processes during past rifting. We know that extensive
50 volcanism and magmatic addition to the Earth's crust occurred during the breakup of
51 Pangea, but we do not fully understand how the distribution changes from north to south
52 along the margin. To study these rocks, which are buried 10 – 20 km beneath the
53 seafloor, we use ocean bottom seismometers that record human made sound waves to
54 determine the sound speed of rocks beneath the surface, which depends on the specific
55 type of rock. We found that the thickness and extent of magma-derived rocks are
56 variable along the margin, with gaps up to 30 km wide. We think that the variability of
57 these rocks is related to processes happening in the continental rift, and that it may
58 have influenced the structure of the Mid-Atlantic Ridge that formed after rifting ended.
59 We also estimate that the total volume of igneous rocks emplaced during breakup is
60 significantly less than previously thought.

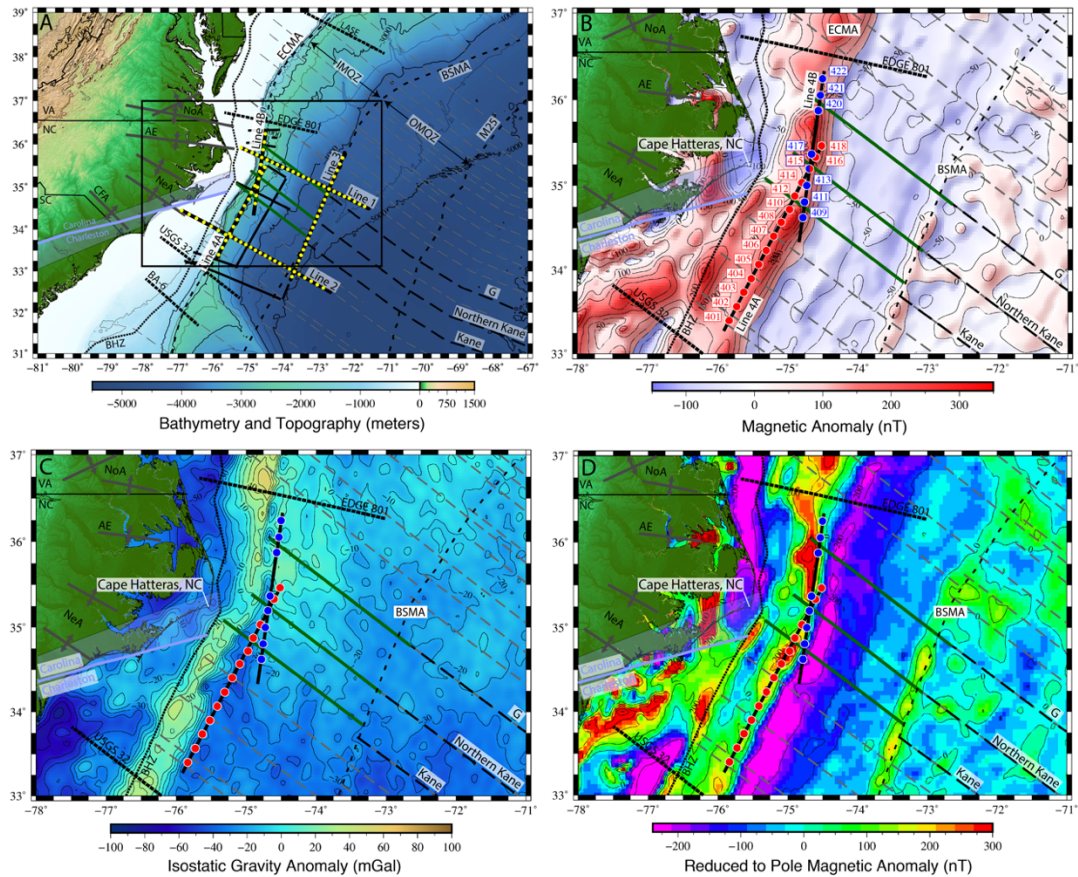
61 **1. Introduction**

62 Volcanic passive margins host significant volumes of igneous addition that are
63 important not only for promoting continental rifting (Bialas et al., 2010; Geoffroy et al.,
64 2015; Thybo & Nielsen, 2009), but also for global environment change and mass
65 extinction events (Marzoli et al., 2018) and the understanding of mantle conditions and
66 processes (e.g. Korenaga et al., 2002; Shuck et al., 2019). The volume and distribution
67 of magmatism and its partitioning between the upper and lower crust during rifting is
68 poorly known because there are limited datasets available to constrain 3D structure at

69 sites of breakup. Along-strike variability in margin structure can offer insight into syn-rift
70 processes and potential connections between margin and mid-ocean ridge
71 segmentation. Strike-perpendicular seismic imaging has constrained along-strike
72 variability at passive margins on larger scales (e.g., Aslanian et al., 2021; Becker et al.,
73 2014; Faleide et al., 2008; Holbrook & Kelemen, 1993; Klingelhoefer et al., 2009;
74 Koopmann et al., 2014), but the paucity of along-strike imaging has prevented the
75 necessary understanding of changes in crustal structure and magmatism along rifts.

76 The Eastern North American Margin (ENAM) is a volcanic passive margin that
77 formed during the breakup of Pangea and opening of the Atlantic Ocean starting at
78 ~200 Ma (Klitgord & Schouten, 1986) (Fig. 1). Crustal structure of the ENAM reflects the
79 conditions of continental breakup, with records of extension and magmatism frozen into
80 the current lithospheric structure. The ENAM has been considered an archetype for
81 volcanic margins based on strike-perpendicular crustal structure containing seaward
82 dipping reflectors (SDRs) and high velocity lower crust (HVLC; >7.2 km/s), which are
83 both interpreted as igneous addition to the margin during rifting (e.g., Austin et al., 1990;
84 Bécél et al., 2020; Holbrook & Kelemen, 1993; Shuck et al., 2019). The East Coast
85 Magnetic Anomaly (ECMA), a large, positive amplitude anomaly that follows the ENAM
86 from Florida to Nova Scotia, is sourced from the volcanic SDR package in the upper
87 crust and has been interpreted as the rift-to-drift transition separating continental and
88 oceanic crust (Alsop & Talwani, 1984; Behn & Lin, 2000; Davis et al., 2018; Greene et
89 al., 2017) (Fig. 1). Along-strike variations in the width and amplitude of the ECMA
90 suggest corresponding changes in rift structure and magmatism, potentially related to

91 segmentation of the Mid-Atlantic Ridge (Behn & Lin, 2000; Greene et al., 2017, 2020)
92 (Fig. 1).



93 **Figure 1) Maps of the ENAM CSE study area with regional geologic and geophysical features.**
94 *A)* Bathymetry and topography shown with the full ENAM CSE survey. Multichannel seismic
95 reflection lines are shown by black solid lines, short period ocean bottom seismometer deployments
96 are shown by yellow circles, and legacy seismic experiment lines EDGE-801, BA-6, USGS 32 and
97 LASE are shown as black labeled lines. Fracture zone extrapolations of Klitgord and Schouten
98 (1986) are shown as gray dashed lines and interpreted inner magnetic quiet zone offsets from
99 Greene et al. (2017) are shown as green lines. Anomaly M25, the Blake Spur Magnetic Anomaly
(BSMA), the Inner Magnetic Quiet Zone (IMQZ), and the Outer Magnetic Quiet Zone (OMQZ) are
labeled. Onshore basement arches and the Carolina-Charleston terrane boundary are labeled. Black
box represents the extent of the other maps. *B)* Zoom in on lines 4A and 4B of the survey with OBS
instrument number labeled. Map shows EMAG2V3 (Meyer et al., 2017). *C)* Isostatic Gravity Anomaly
(Behn and Lin, 2000). *D)* Reduced to Pole (RTP) magnetic anomaly (Behn and Lin, 2000).

100 In this study, we use traveltome tomography to model the P-wave velocity
101 structure beneath the ECMA for a ~370-km-long along-strike section centered on Cape
102 Hatteras, North Carolina. These models and subsequent analyses based on the velocity

103 structure offer insight into the crust beneath the ECMA and delineate along-strike
104 variability in crustal structure at scales of ~30 km which reflect early rifting structures.

105 **1.1 Synrift Magmatism**

106 Igneous addition at continental rifts is often characterized by extensive surface
107 volcanism with localized intrusions into the crust or underplating at the base of the crust
108 (Bastow & Keir, 2011; Ebinger & Casey, 2001; Keranen et al., 2004; Thybo &
109 Artemieva, 2013). Synrift magmatism accommodates some extensional strain during
110 breakup and may be necessary for rifting, as modeling indicates that plate boundary
111 forces alone are too weak to break apart intact continental lithosphere (Bialas et al.,
112 2010; Buck, 2006). Igneous addition at volcanic margins, including the ENAM, the West
113 African Conjugate Margin, the southern West African Margin, and the South American
114 Margin, has been interpreted as a combination of volcanic flows (i.e., the SDRs) and
115 magmatic intrusions or underplating (i.e., the HVLC) (e.g., Aslanian et al., 2021; Becker
116 et al., 2014; Faleide et al., 2008; Holbrook & Kelemen, 1993; Klingelhoefer et al., 2009;
117 Koopmann et al., 2014).

118 Previous studies of the ENAM interpolated between widely spaced margin-
119 perpendicular profiles and assumed long wavelength (100 - >1000 km) along-strike
120 variability of crustal structure (Holbrook & Kelemen, 1993). However, smaller
121 wavelength (<100 km) variability in the magnitude and width of the ECMA implies that
122 there is significant variability in the thickness and extent of the anomaly's source body,
123 thought to be the SDR package, on smaller scales (Behn & Lin, 2000; Davis et al.,
124 2018; Greene et al., 2020). Recent magnetic modeling along the whole margin
125 interpreted multiple scales of magmatic segmentation along the margin based on

126 variability of the SDR package (Greene et al., 2020) (Fig. 1). In the vicinity of Cape
127 Hatteras, NC, the magnetic source body changes broadly from thinner and wider in the
128 south to thicker and narrower to the north, implying that Cape Hatteras is an important
129 boundary along the margin (Greene et al., 2020). Constraining the full crustal structure
130 beneath the ECMA has been difficult because there has been a lack of along-strike
131 imaging at the ENAM and magnetic modeling does not offer insight into the lower crust.
132 Along-strike imaging can illuminate variabilities in the lower crust at similar scales to
133 those in the upper crust observed by whole margin modeling; if the SDRs and the HVLC
134 were connected by the same magmatic plumbing system, we would expect significant
135 variability in the thickness and extent of the HVLC correlated with SDR variability.

136 **1.2 Segmentation of the ENAM**

137 The relationship between segmentation of continental rifts and mature mid-ocean
138 ridges remains unclear, but the crustal structure at rifted margins may hold crucial
139 evidence that that connects them (Behn & Lin, 2000; Gerya, 2013; Greene et al., 2017;
140 Illsley-Kemp et al., 2018; Taylor et al., 2009; Thomas, 2006). Continental rifts exhibit
141 magmatic segmentation with sporadic intrusion and volcanism and/or structural
142 segmentation with distinct fault systems (e.g., Ebinger & Casey, 2001; Hammond et al.,
143 2011; Hayward & Ebinger, 1996). Mid-ocean ridge systems have characteristic
144 segmentation with spreading segments bounded by oceanic transform faults that
145 become fracture zones away from the ridge axis (Schouten et al., 1985). Rift
146 segmentation may carry over to mature spreading centers based on the long
147 wavelength variability of margin anomalies (Behn & Lin, 2000; Wyer & Watts, 2006),
148 modeling of fracture zone formation (Gerya, 2013; Illsley-Kemp et al., 2018; Taylor et

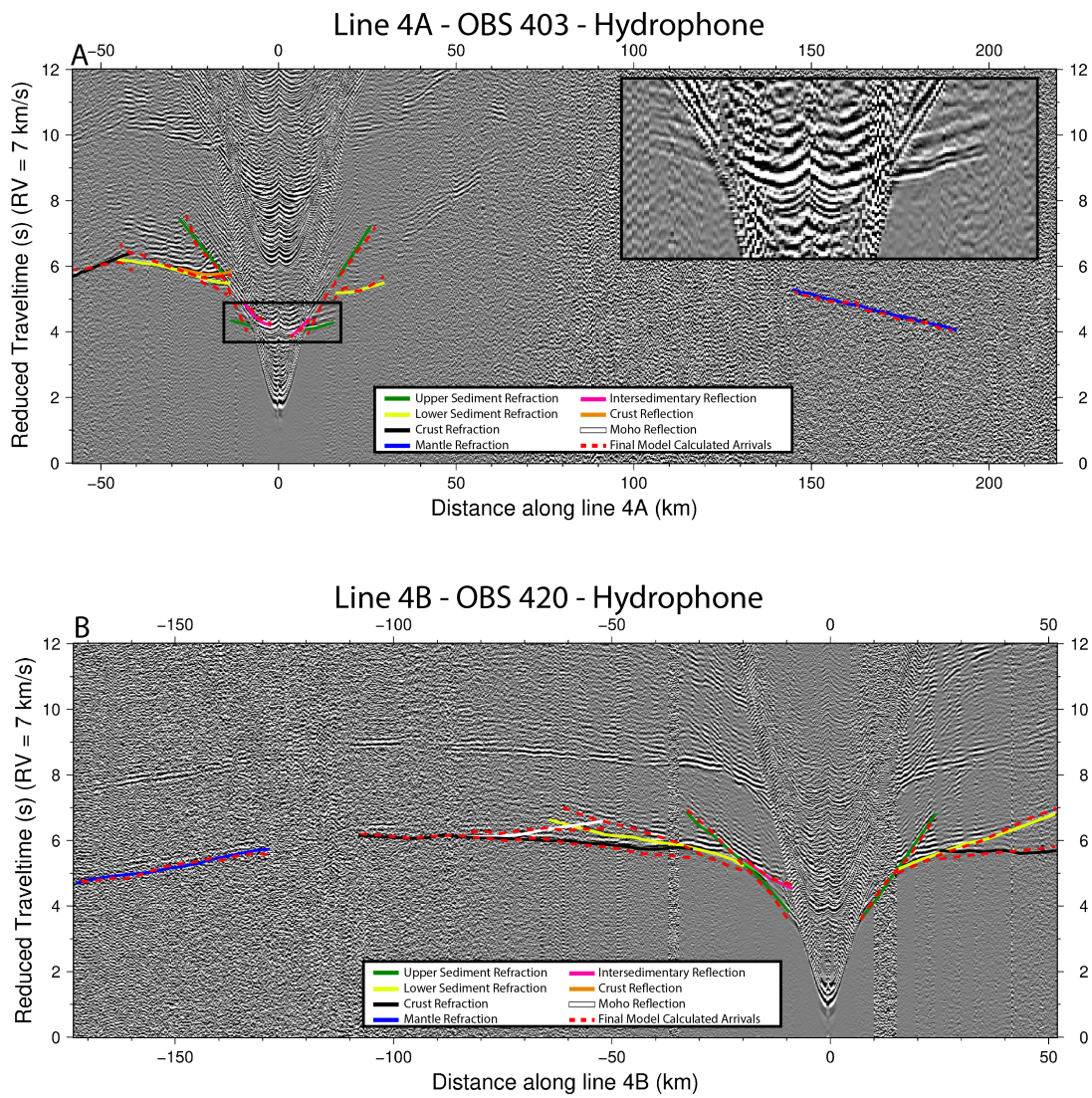
149 al., 1995), structural correlation through multiple Wilson cycles (Thomas, 2006), or
150 correlation between onshore and offshore structures (e.g., Franke et al., 2007;
151 Koopmann et al., 2014).

152 The ECMA magnetic signature shows segmentation at multiple wavelengths
153 (~600 – 1000 km and ~50 – 100 km) that may correlate with Mid-Atlantic Ridge
154 segmentation (Greene et al., 2020). Along-strike segmentation of the SDR package
155 interpreted in the south Atlantic margins and variability observed in the West African
156 Coast Magnetic Anomaly also suggest a connection (Biari et al., 2017; Franke et al.,
157 2007; Klingelhoefer et al., 2009; Koopmann et al., 2014). Relating structures along the
158 ENAM to Mid-Atlantic Ridge segmentation is difficult because of the Atlantic Jurassic
159 Quiet Zone, a region between M25 and the ECMA with no observable seafloor magnetic
160 lineations (Behn & Lin, 2000; Greene et al., 2017) (Fig. 1). The combined lack of
161 lineations and thicker abyssal sediments prevent tracing of Mid-Atlantic Ridge fracture
162 zones in this region, so linear extrapolations based on plate motion have been used to
163 approximate their locations at the ECMA (Behn & Lin, 2000). Recent analysis of the
164 Inner Magnetic Quiet Zone (IMQZ) found faint lineations with offset that correspond to
165 some extrapolated fracture zones, suggesting that there may be some segmentation
166 structures at the ECMA that could be seismically imaged (Greene et al., 2017) (Fig. 1).
167 Shuck et al. (2019) found no correlated structures along the Blake Spur Magnetic
168 Anomaly, an indication that segmentation of the Mid-Atlantic Ridge may have developed
169 after full lithospheric rupture. Previous to our study, magmatic segmentation at the
170 ECMA was implied by Greene et al. (2020), but it remains unclear whether this early
171 segmentation is recorded in the lower crustal structure.

172 **2. Data and Methods**

173 **2.1 ENAM-CSE Line 4A and 4B**

174 For this study we used ocean bottom seismometer (OBS) data from 23 stations
175 acquired as part of the NSF-funded Eastern North American Margin Community
176 Seismic Experiment (ENAM-CSE) in 2014 (Van Avendonk, 2015; Lynner et al., 2019).
177 The OBSs recorded shots from the 36-element, 6600-in³ array of the *R/V Marcus G.*
178 *Langseth* along each profile (Fig. 1). We focus on Lines 4A and 4B located within the
179 peak of the ECMA following the margin along-strike for ~370 km (Fig. 1). OBS gathers
180 used for this study generally have a high signal to noise ratio with multiple arrivals
181 evident and energy arriving from up to ~200 km offsets (Fig. 2). Stations A401-A406
182 have more complex arrivals within short offsets (< +-40 km) and have a near-offset first
183 arrival with an apparent velocity of 6 km/s (much faster than typical sediment velocities)
184 (Fig. 2). Picking arrivals between ~40 km and ~125 km source-receiver offset on
185 stations A401-A406 was difficult due to low amplitudes and low coherency (Fig. 2). We
186 attempted to include these arrivals in the inversions, but it was difficult to distinguish
187 consistent phases and corresponding layer geometry, so only the first arriving, high
188 energy phases were included in this area (Fig. 2). At offsets greater than ~125 km on
189 these OBSs, amplitudes and coherency returned to normal levels and arrivals could be
190 identified and picked (Fig. 2).



191
192
193
194

Figure 2) **Annotated ocean bottom seismometer data.** An OBS gather from Line 4A (station 403) (A) and Line 4B (station 420) (B) of the ENAM CSE plotted in distance along the line and reduced traveltime (with reduction velocity of 7 km/s). Traveltime picks (multicolor - see legend) and final calculated arrivals (red dashed) are plotted on top of data. Inset is an unpicked zoom onto the early, fast arrival caused by salt diapirism found on the southern end of line 4A.

195
196
197
198
199

We used a Butterworth bandpass filter on the OBS gathers to target frequencies between 4 and 15 Hz for general phase identification and interpretation, and between 10 and 25 Hz for near offset reflections. We identified seven phases for use in the velocity inversion that are similar to other recent refraction studies from the ENAM-CSE (i.e., Shuck et al., 2019), including an upper sedimentary refraction (Ps1), a lower

200 sedimentary refraction (Ps2), a crustal refraction (Pg), an upper mantle refraction (Pn),
201 an inter-sedimentary reflection (PsP), a reflection from the top of the crust (PgP), and a
202 Moho reflection (PmP). Uncertainties were assigned to all picked arrivals, ranging from
203 75 – 125 ms, based on source-receiver offset and visual inspection of signal-to-noise
204 ratio. We used forward modeling of picks from each station and verified arrival
205 reciprocity to quality control our traveltimes before inversion.

206 **2.2 Traveltime Tomography**

207 We performed traveltimes tomography with VMTomo following the methods of
208 Van Avendonk et al. (2004) to iteratively invert our traveltimes picks for subsurface P-
209 wave velocities and boundary layer geometry. Our simple starting velocity models were
210 based on results from crossing Lines 1 and 2 (Shuck et al., 2019) taken at the
211 intersection points with Lines 4A and 4B and hung from the seafloor (Suppl. Fig. 1).

212 VMTomo first calculates raypaths and their respective traveltimes for each phase
213 per shot point-OBS pair. The calculated travel times are compared to the corresponding
214 picked traveltimes, and the inversion then seeks to minimize the travel time residual by
215 updating the velocity structure. The models were both constructed with 0.5 km by 0.2
216 km grid cells with no depth dependent changes in size. We chose a raytracing search
217 radius of 0.2 km to match the vertical grid size and prescribed a regularization area of
218 20 km by 0.4 km with higher relative smoothing and a balanced regularization between
219 boundary depths and velocities. In our analyses, the χ^2 error metric was decreased by
220 ~50% with each iteration until a value of ~1 (indicating that the model misfit matches the
221 prescribed uncertainty) was reached. We chose to apply a layer stripping approach,
222 where we first inverted the shallowest layer to a χ^2 of 1 then moved to the next deepest

223 layer while holding everything above fixed. We verified the χ^2 of the entire model by
224 running a final iteration with every phase at once.

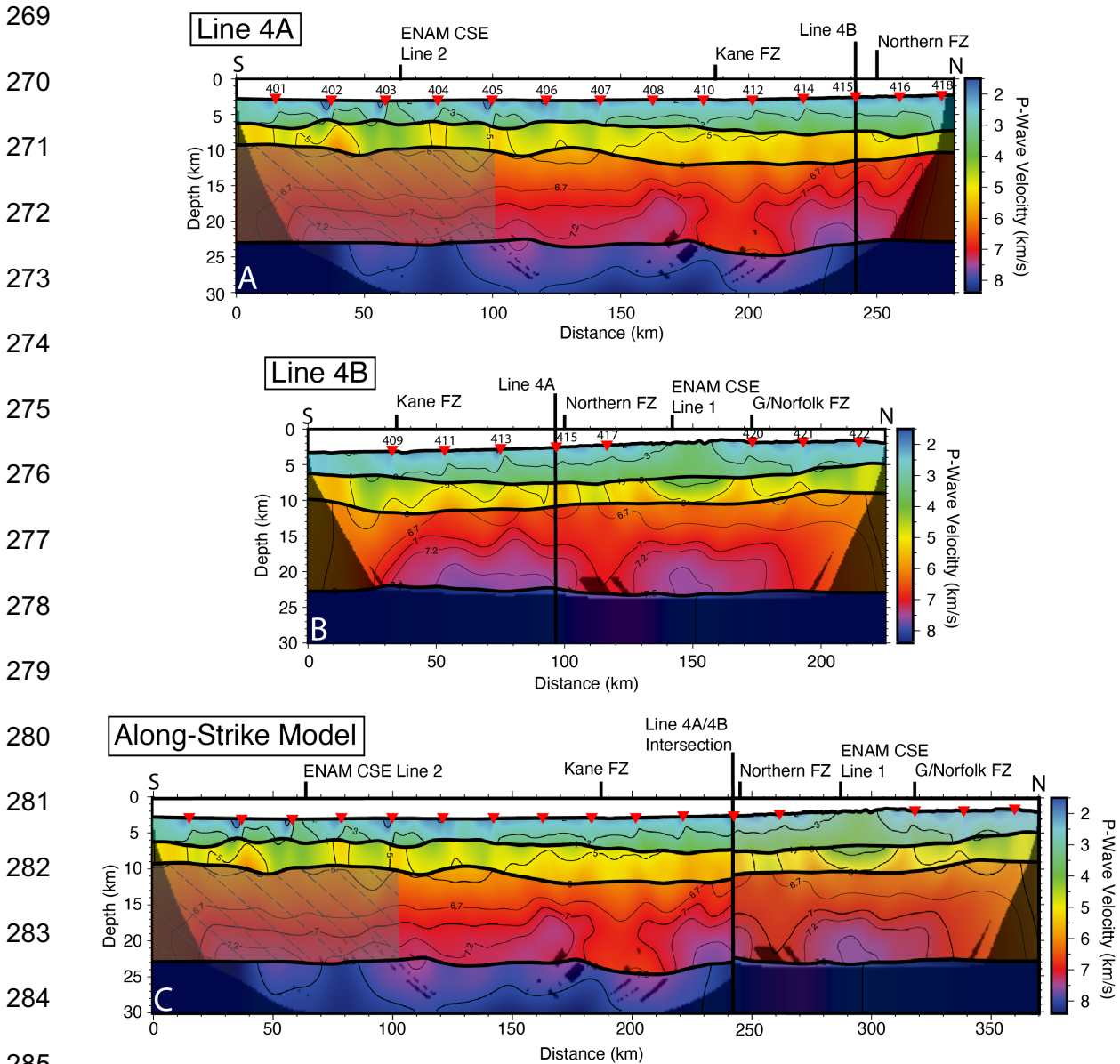
225 We performed resolution tests and calculated derivative weight sum (DWS) on
226 both velocity models to help guide our interpretations (Suppl. Figs. 2,4,5,6). Resolution
227 results greater than ~50% for a given size test ellipse are considered acceptable for
228 active source tomography of this kind (Van Avendonk et al., 2004). With the ray
229 coverage for each line, the velocity models can reliably resolve large scale features
230 (represented by an ellipse of 60 km by 8 km) on both lines within the sedimentary and
231 crust layers except for the region between 0 and 100 km along Line 4A that has
232 significantly low ray coverage (Suppl. Figs. 2,6). The velocity models can also reliably
233 resolve small (10-km wide by 2-km tall) and medium scale features (30-km wide by 5-
234 km tall) in the sedimentary layers and can resolve medium scale features in the crustal
235 layer (Suppl. Figs. 4,5).

236 We estimated the uncertainty in our modeled crustal velocities and in the Moho
237 velocity-depth tradeoff by perturbing our final model, raytracing the corresponding
238 phases, and calculating a new χ^2 . The crustal velocities have acceptable χ^2 values (\leq
239 1.25) with perturbations from -0.05 – 0.07 km/s (Line 4A) and from -0.06 – 0.045 km/s
240 (Line 4B) (Suppl. Figs. 7,8). For the velocity-depth tradeoff, the Moho reflection phase
241 (PmP) has acceptable χ^2 values (\leq 1.25) with depth perturbations from -0.28 – 0.85 km
242 (Line 4A) and -1.5 – 0.78 km (Line 4B) and with velocity perturbations from -0.07 – 0.27
243 km/s (Line 4A) and from -0.2 – 0.29 km/s (Line 4B) (Suppl. Figs. 9,10).

244 **3. Results**

245 The final velocity models for Lines 4A and 4B have χ^2 values of 1.12 and 1.18,
246 respectively, with RMS misfits of 101 and 108 ms (Fig. 3). The upper sedimentary layer
247 on both lines has velocities ranging from 1.8 to 3.9 km/s and thicknesses ranging from
248 ~2.0 to ~5.5 km. On Line 4A, between 0 km and 100 km along-strike, there are
249 anomalously low velocities coincident to the OBS locations and a highly variable along-
250 strike structure which we believe is due to previously identified salt diapirs that were
251 observed on MCS reflection profiles (Dillon et al., 1982; Shillington et al., 2014; Tréhu et
252 al., 1989) (Fig. 3). The low-quality data on OBS A401-A406 and the low ray coverage
253 on the southern end of Line 4A are likely the result of these diapirs with very high
254 seismic velocities relative to the surrounding sediment (Figs. 2,3 Suppl. Figs. 4,5,6).
255 The lower sedimentary layers have velocities ranging from 2.9 to 5.9 km/s with
256 thicknesses ranging from ~2.7 to ~5.0 km (Fig. 3). The crustal layers have velocities
257 from 5.9 to 7.6 km/s with thicknesses from ~10.0 to ~13.0 km (Fig. 3). Velocities in the
258 crustal layers have more along-strike variability than the other layers, including two
259 anomalously low velocity regions between ~180 and ~210 km on Line 4A and between
260 ~105 and ~130 km on Line 4B where velocities just above the Moho only reach 6.9 to
261 7.0 km/s (Fig. 3). Within the upper mantle, velocities range from 7.9 to 8.1 km/s with
262 minimal along-strike variation. The layer boundary depths and seismic velocities
263 generally agree with previous tomography results in other parts of the margin (e.g.
264 Austin et al., 1990; Holbrook & Kelemen, 1993; LASE Study Group, 1986; Shuck et al.,
265 2019). At the intersection point with Line 1 and Line 2 from the ENAM-CSE, the Moho
266 on Lines 4A/4B is ~1-2 km deeper, which may represent slight differences in modeling

267 parameters (Shuck et al., 2019) or tradeoffs between lower crustal velocity and Moho
 268 depth (Suppl. Figs. 9,10).



286 Figure 3) **Velocity modeling results.** Velocity models from Line 4A (A), Line 4B (B), and a combined
 287 along-strike model (C). P-wave velocities in each model are contoured and correspond to the color bar.
 288 Shaded and hatched region on Line 4A covers section of igneous crust with low ray coverage and
 289 resolution due to overhead salt diapirs. The combined along-strike velocity model was made with the
 portion of line 4A south of the intersection point and line 4B north of the intersection point.

290 To generate an along-strike view of the margin, we combined Lines 4A and 4B at
291 their intersection point near Cape Hatteras, NC (Figs. 1,3). At the intersection point,
292 velocities and boundary depths are in close agreement (Fig. 3). For this ~370-km-long
293 section of the margin, the most along-strike variability is contained within the crustal layer.
294 There is a slight thickening trend in the total crustal thickness and total sediment
295 thickness from south to north, but this appears predominately related to shallowing
296 bathymetry and the slight upslope orientation of Line 4B (Fig. 3, Suppl. Fig. 11). The
297 lower velocity regions in the lower crust on Lines 4A and 4B at distances of ~180 km to
298 ~210 km and ~245 km to ~285 km in the combined model are similar in size, but the
299 area on Line 4B has a slightly higher velocity (6.9 km/s vs 7.1 km/s) (Fig. 3).

300 **4. Discussion**

301 **4.1 Interpretation of the Velocity Model**

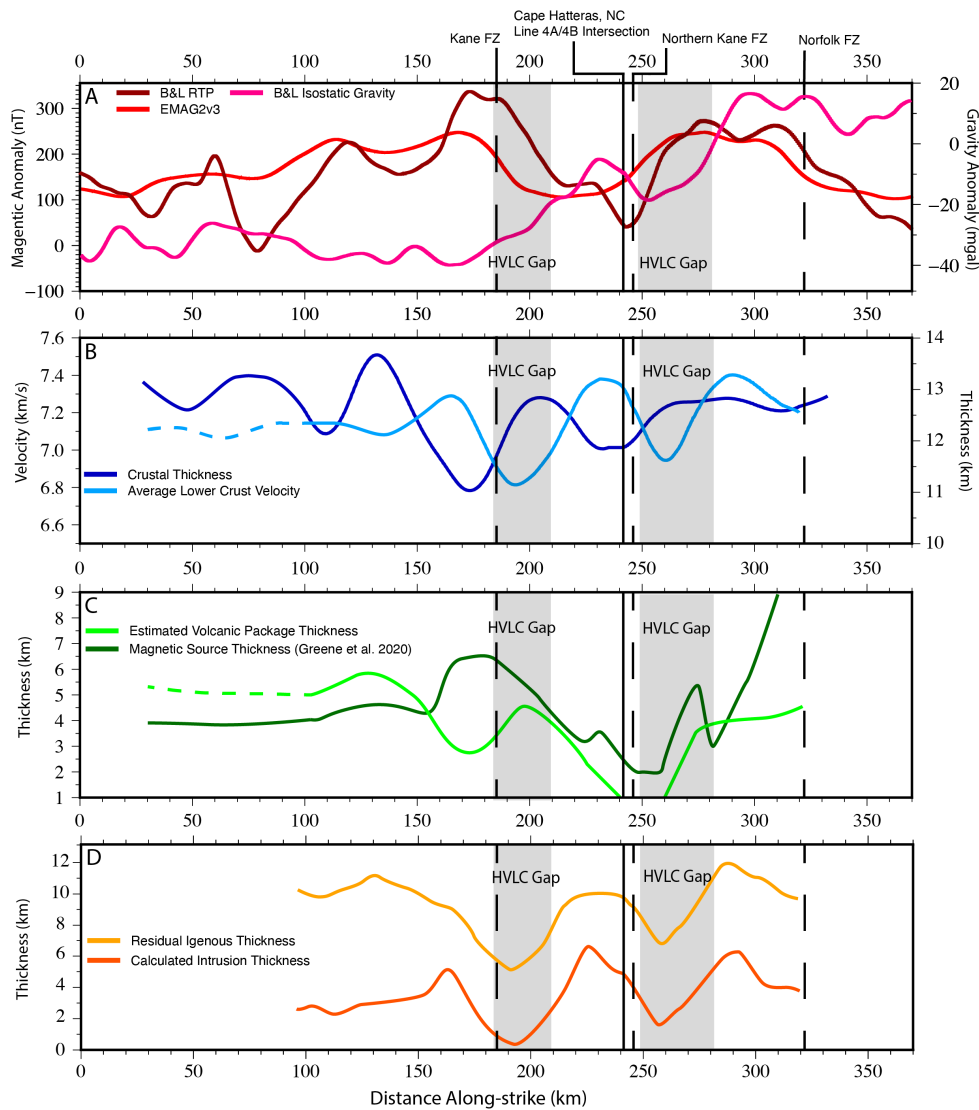
302 The new P-wave velocity models along Lines 4A and 4B show detailed along-
303 strike crustal structure beneath the ECMA for the first time, revealing significant
304 variations in lower crustal velocity. The upper crustal velocity structure is also laterally
305 heterogeneous, but changes in upper and lower crustal velocities are not tightly
306 correlated. Our results fill in gaps between previous, sparse margin perpendicular
307 observations and offer new insight into igneous addition during rifting and continental
308 breakup.

309 To interpret igneous materials beneath the ECMA, we used isovelocity contours
310 to approximate the areas of extrusive and intrusive addition. We use velocity contours
311 as our best approximation for because there were no reflections observed in the OBS
312 data that could delineate packages within the crust layer (Fig. 2) and initial processing

313 of coincident MCS reflection profiles from Lines 4A and 4B (Shillington et al., 2014)
314 showed little reflectivity within the basement that could be used to define boundaries. At
315 other volcanic margins, a lack of a mid-crustal reflection has been an indicator of
316 intrusion into the lower crust during rifting as opposed to underplating at the base of the
317 crust (Bécel et al., 2020; Eddy et al., 2014; Shuck et al., 2019; White et al., 2008).
318 Combined analysis of the wide-angle tomography results and MCS reflection profiles
319 from ENAM-CSE Lines 1 and 2 (Bécel et al., 2020; Shuck et al., 2019) show that the
320 upper portion of the SDR package in the MCS profile sits between the top of the crust
321 layer and the 6.5 km/s contour of the velocity model but these models did not image the
322 definitive base of the package. Along-strike variations in overburden can affect the
323 seismic velocities within the crust, we observe only small changes in sediment thickness
324 along-strike so this effect would be minimal (Fig. 3, Suppl. Fig. 11). Our uncertainty
325 analysis indicates that crustal velocities are well constrained with a depth uncertainty of
326 $\sim\pm 0.5$ km. Therefore, we use isovelocities to illuminate relative changes in both the
327 thickness of the volcanic layer and in the amount of synrift magmatic addition to the
328 lower crust in place of having a defined boundary.

329 Following previous investigators (e.g., Holbrook and Keleman, 1993; Shuck et
330 al., 2019), we used the 6.7 km/s contour to estimate the base of the extrusive (volcanic)
331 package and 7.2 km/s to estimate the top of the HVLC. With our isovelocity based
332 interpretation scheme, a volcanic package is present across both Lines 4A and 4B, with
333 a notable region between 210 km and 270 km along-strike where the 6.7 km/s contour
334 shallows to meet the top of the crust indicating significant thinning. HVLC is present on
335 both profiles except for two regions, from 170 – 220 km and 250 – 270 km in the along-

336 strike model, which have velocities less than ~ 7.2 km/s. We categorize these regions in
 337 the lower crust with reduced velocities as HVLC “gaps” because of the previously
 338 assumed prevalence of HVLC at the magma-rich ENAM (Fig. 3).



339
 340 Figure 4) **Along-strike analysis.** Vertical lines show the location of the line 4A/4B intersection point,
 341 Cape Hatteras, NC, and the Kane, Northern Kane, and Norfolk fracture zones. Vertical gray boxes represent
 342 location of the HVLC gaps. A) Geophysical anomalies coincident to our along-strike model including
 343 EMAG2V3, the RTP magnetic anomaly from Behn and Lin (2000), and the isostatic gravity anomaly from
 Behn and Lin (2000). B) Crustal thickness along-strike, calculated from the top of the crust layer to the
 Moho and the average lower crustal velocity. C) Estimated volcanic package thickness, calculated from the
 top of the crust to the 6.7 km/s velocity contour and the modeled magnetic source thickness from Greene
 et al. (2020). D) Calculated intrusion thickness into the lower crust based on the linear mixing calculation
 of Marzen et al. (2020) and the residual igneous thickness determined by adding the intrusion thickness
 to the volcanic thickness (light green line in C).

344 To further contextualize our results, we compare with regional potential fields
345 data (Fig. 4). The two-dimensional velocity models we present do not capture variable
346 3D structure that contributes to the potential fields, such that correlations between the
347 two may be imperfect, but some general correlations may be expected. Magnetic and
348 gravity anomalies along the ENAM show significant along-strike variation in amplitude
349 (Figs. 1,4) that should reflect changes in the magnetic source body and density
350 structure, respectively (e.g., Behn & Lin, 2000; Greene et al., 2020; Wyer & Watts,
351 2006). For the regions where we have reliable resolution, the reduced-to-pole (RTP)
352 magnetic anomaly appears to broadly be positively correlated with the estimated
353 volcanic thickness calculated from the top of the crustal layer to the 6.7 km/s contour
354 (Behn & Lin, 2000) (Fig. 4). The general correlation is consistent with the volcanic
355 package constituting the primary magnetic source (Austin et al., 1990; Davis et al.,
356 2018; Greene et al., 2017, 2020). In terms of gravity, the northern HVLC gap correlates
357 with a local minimum in the isostatic gravity anomaly but the southern HVLC gap does
358 not (Behn & Lin, 2000) (Fig. 4). The isostatic anomaly should be sensitive to variations
359 in density structure throughout the sediments, crust, and upper mantle, so the lack of
360 correlation with the southern HVLC gap could be due to its location within a larger trend
361 of decreasing gravity anomaly or 3D structures influencing the anomaly that that our 2D
362 lines cannot capture (Fig. 4).

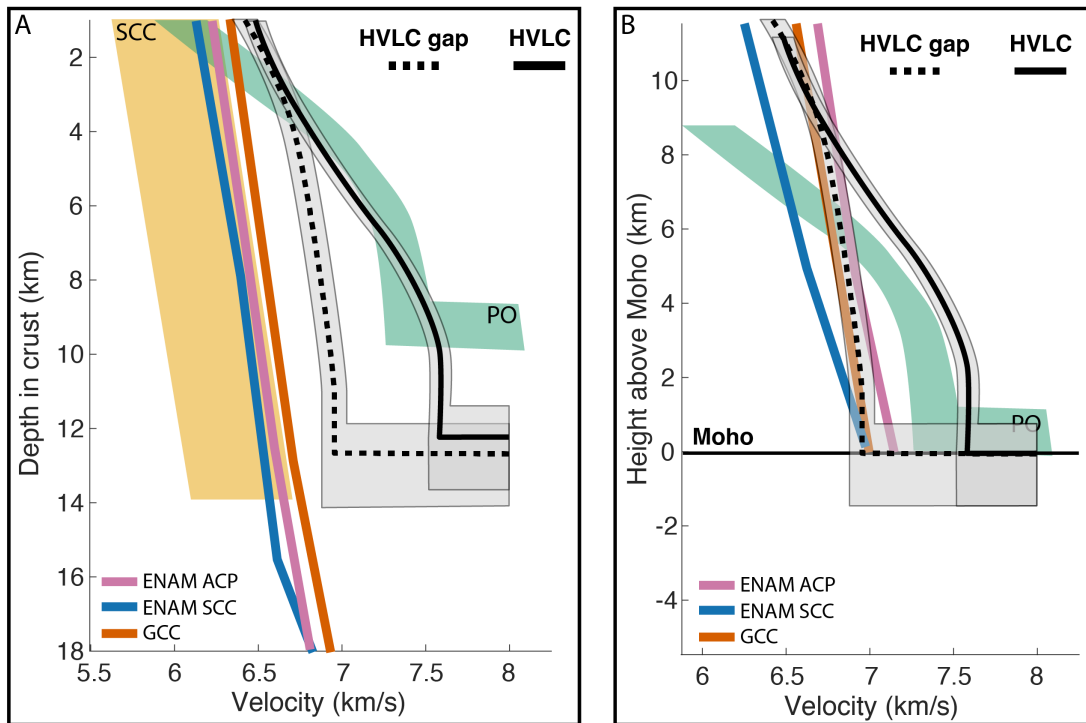
363 We also note that the estimated volcanic and HVLC thicknesses are not
364 correlated along-strike (Figs. 3,4). For example, south of the 4A/4B intersection a thick
365 section of volcanics overlies a section of crust without HVLC (Fig. 4). This observation is
366 surprising because both surface volcanics and the HVLC represent igneous addition to

367 the margin derived from the same mantle melt, so we might expect to find the thickest
368 volcanic sections above the thickest HVLC. Cape Hatteras, NC (coincident to the
369 intersection point) represents a change in margin orientation (Fig. 1), early seafloor
370 spreading regimes (Greene et al., 2017), and early rifting processes (Greene et al.,
371 2020), but it is difficult to know if those long wavelength variations would affect the
372 small-scale structure. While the upper and lower crust are both sourced from the same
373 mantle melt, and they are correlated on larger scales (>500 km), our results suggest
374 that the magmatic system is more complex at smaller scales.

375 **4.2 Origin of the Lower Crust Beneath the ECMA**

376 Previous studies that detected HVLC beneath the ECMA had considered it a
377 continuous, tabular shaped feature for the length of ENAM (e.g., Holbrook & Kelemen,
378 1993). Considering the distribution of HVLC in our along-strike view and in the models
379 from ENAM-CSE Lines 1 and 2 (Shuck et al., 2019), we suggest instead that the HVLC
380 may be more sporadically distributed along the margin. However, the origin of this
381 along-strike variability remains unclear. The crust beneath the ECMA is sandwiched
382 between the extended continental crust of the Atlantic coast plain (Luckie, 2017; Guo et
383 al., 2019) and continental shelf (Shuck et al., 2019) and anomalously thin, faulted, and
384 seismically fast proto-oceanic crust (Bécel et al., 2020; Shuck et al., 2019). Bécel et al.,
385 (2020) interpreted the crust beneath the ECMA as extrusive upper crust with
386 intermediate diking and lower crustal intrusion based on ENAM-CSE MCS profiles Lines
387 1 and 2 (Fig. 1), combined with collocated the wide-angle tomography (Shuck et al.,
388 2019). Many other passive margins show similar structure based on strike-
389 perpendicular seismic profiling (e.g Aslanian et al., 2021; Biari et al., 2017; Klingelhoefer

390 et al., 2009; Museur et al., 2021; White et al., 2008). Our observation that HVLC
 391 beneath the ENAM is discontinuous on ~30-km length scales, however, has not been
 392 observed at other margins with along-strike profiles (e.g., Aslanian et al., 2021;
 393 Contrucci et al., 2004; Klingelhofer et al., 2009; Reuber et al., 2016).



394 Figure 5) **One Dimensional Analysis.** Plots of the average 1D velocity profiles comparing the crust
 395 with HVLC and the crust with HVLC gaps to stretched continental crust (SCC) (Christensen and Mooney,
 396 1995), proto-oceanic crust (PO) (Shuck et al., 2019), continental crust from the Atlantic Coastal Plain
 397 (ENAM ACP) (Luckie 2017), continental crust from southern Georgia (GCC) (Marzen et al., 2020), and
 398 stretched continental crust from Line 1 and Line 2 landward of the ECMA (ENAM SCC) (Shuck et al.,
 2019). 1D velocity profiles are hung from their respective top of the crust (A) and are aligned at their
 respective Moho as determined by the authors (B). Gray boxes around the HVLC and HVLC gap profiles
 reflect estimated uncertainties in the model's crustal velocities and Moho depth.

399 To further investigate the nature of the heterogeneous lower crust beneath the
 400 ENAM, we calculated the average velocity-depth profile for crust with and without HVLC
 401 on Lines 4A and 4B. We compared the 1D profiles with the proto-oceanic crust from
 402 Lines 1 and 2 of the ENAM CSE and with a range of continental crust profiles from the
 403 Atlantic Coastal Plain, the ENAM continental shelf, the south Georgia Basin, and a

404 global baseline (Christensen & Mooney, 1995; Luckie, 2017; Marzen et al., 2020; Shuck
405 et al., 2019) (Fig. 5).

406 When hung from the top of the crust, the average one-dimensional velocity-depth
407 profile for sections with and without HVLC have nearly identical upper crustal velocities
408 that are close to the upper proto-oceanic crust, which would also have a volcanic origin
409 (Fig. 5A). Velocities near the top of the crust are slightly higher than the equivalent
410 proto-oceanic crust, but this difference could be due to the thicker sediment load
411 beneath the ECMA closing fractures and raising the velocity (Fig. 5A). At ~4 – 5 km
412 depth, the HVLC profile diverges, reaching ~7.5 km/s at the Moho as opposed to ~6.9
413 km/s for crust without HVLC (Fig. 5A). The velocity profile for the HVLC gaps is located
414 in between the proto-oceanic crust and the continental crustal profiles providing an
415 unclear origin (Fig. 5A).

416 To compare lower crustal structure more directly, we align the one-dimensional
417 velocity profiles at the Moho, as interpreted by the authors of each respective study
418 (Fig. 5B). In this view, the HVLC gap profile falls within the range of lower continental
419 crust from eastern North America (Luckie, 2017; Marzen et al., 2020; Shuck et al.,
420 2019), suggesting that these sections represent lower continental crust that was not
421 intruded during rifting (Fig. 5B). Studies at other Atlantic passive margins have found
422 that the middle to lower continental crust may persist through extension becoming the
423 base of transitional margin crust (e.g. Aslanian et al., 2021; Biari et al., 2017; Contrucci
424 et al., 2004; Klingelhoefer et al., 2009). Based on this analysis, we suggest that the
425 along-strike variation in the lower crust velocity structure beneath the ECMA reflects

426 alternating sections of extensive and limited intrusion into lower continental crust (Fig.
427 6).

428 **4.3 Igneous Addition During Continental Breakup**

429 Volcanic margins are defined by a significant volume of igneous addition, and
430 several previous studies have attempted to calculate the ENAM's total igneous volume.
431 We first use our interpreted velocity models to approximate the proportion of extrusive
432 and intrusive magmatism at the ENAM as this ratio is frequently used to estimate the
433 total volume for the margin. A recent global analysis of volcanic rifted margins found an
434 average thickness ratio of 1:3 between SDRs and HVLC, providing a baseline value for
435 the ratio of extrusive to intrusive rocks (Gallahue et al., 2020). Observations in both
436 active and failed rifts (e.g., the Midcontinent Rift (Elling et al., 2020), the Afar Rift
437 (Bastow & Keir, 2011), and the Main Ethiopian Rift (Keranen et al., 2004)) and at
438 volcanic passive margins (e.g., offshore Norway (Faleide et al., 2008), South America
439 (Becker et al., 2014), and southwest Africa (Koopmann et al., 2014)) indicate that
440 SDR:HVLC thickness ratios may vary along-strike, but there has not been a detailed
441 along-strike analysis of the ratio at the ENAM.

442 By comparing our isovelocity derived thicknesses (e.g., Fig. 4), we find that the
443 ratio between the volcanics and the HVLC in this part of the ENAM is $1:2 \pm 0.25$ on
444 average. However, this estimate assumes that the entire lower crust is fully formed from
445 igneous addition, not heavily intruded continental crust. To refine our estimate, we
446 calculated the along-strike igneous intrusion thickness into the crust using a linear
447 mixing equation following the methods of White et al. (2008) and Marzen et al. (2020)
448 (Fig. 4). Assuming a background lower crustal velocity of 6.8 km/s and a mafic intrusion

449 velocity of 7.5 km/s, the intrusion thickness ranges from ~0.5 km to ~6.5 km with local
450 minimums coincident to the HVLC gaps (Fig. 4). Adding the estimated volcanic package
451 thickness to the calculated intrusion thickness represents the total igneous thickness
452 along-strike, which varies more significantly than the overall crustal thickness (Fig. 4).

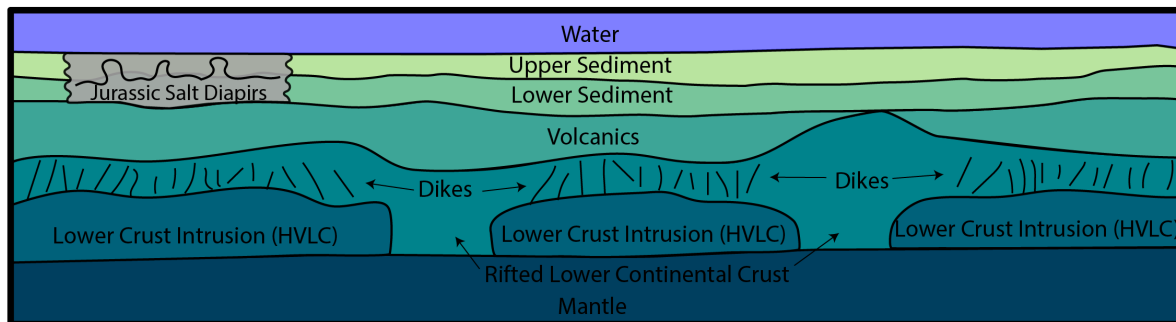
453 The updated intrusion thickness reduces the extrusive:intrusive ratio to
454 1:1.25±.25 which is similar to the ratio determined by White et al. (2008) in the North
455 Atlantic. Without a modeled reflector separating the volcanics and HVLC, our ratio is
456 dependent on the specific isovelocity chosen as the proxy boundary. A different chosen
457 velocity would result in a slightly different ratio, but our results indicate that the ratio is
458 generally lower than previous estimates from ENAM and the recent global compilation
459 from Gallahue et al. (2020).

460 Holbrook & Kelemen (1993) calculated a maximum igneous volume of $\sim 3.2 \times 10^6$
461 km^3 using the cross-sectional area of imaged SDRs and HVLC on transects BA-6 and
462 EDGE 801 multiplied by the margin length (Fig. 1). Greene et al. (2020) modeled the
463 margin-wide ECMA magnetic source and used the SDR:HVLC relation of Gallahue et
464 al. (2020) (SDR:HVLC = 1:3) to estimate a total volume of $\sim 1.6 \times 10^6 \text{ km}^3$, a 50%
465 reduction. While the Greene et al. (2020) estimate accounts for variability along the
466 margin, it relies on a global relationship that may not apply to the ENAM. Using our new
467 calculated ratio along the entire margin, the Greene et al. (2020) estimate would reduce
468 by ~48% to $8.39 \pm 0.93 \times 10^5 \text{ km}^3$. In addition to the updated ratio, the observed
469 discontinuities in HVLC along the rest of the margin would further reduce the volume by
470 a potentially significant amount. However, it remains unclear how prevalent the HVLC
471 discontinuities are along the ENAM. These volume estimates are not definitive, but add

472 to a growing body of evidence that magmatism during the formation of the ENAM was
473 less voluminous and more irregularly distributed than previously thought (e.g., Bécél et
474 al., 2020; Greene et al., 2020; Marzen et al., 2020; Shuck et al., 2019)

475 **4.4 Magmatic Segmentation During Early Rifting**

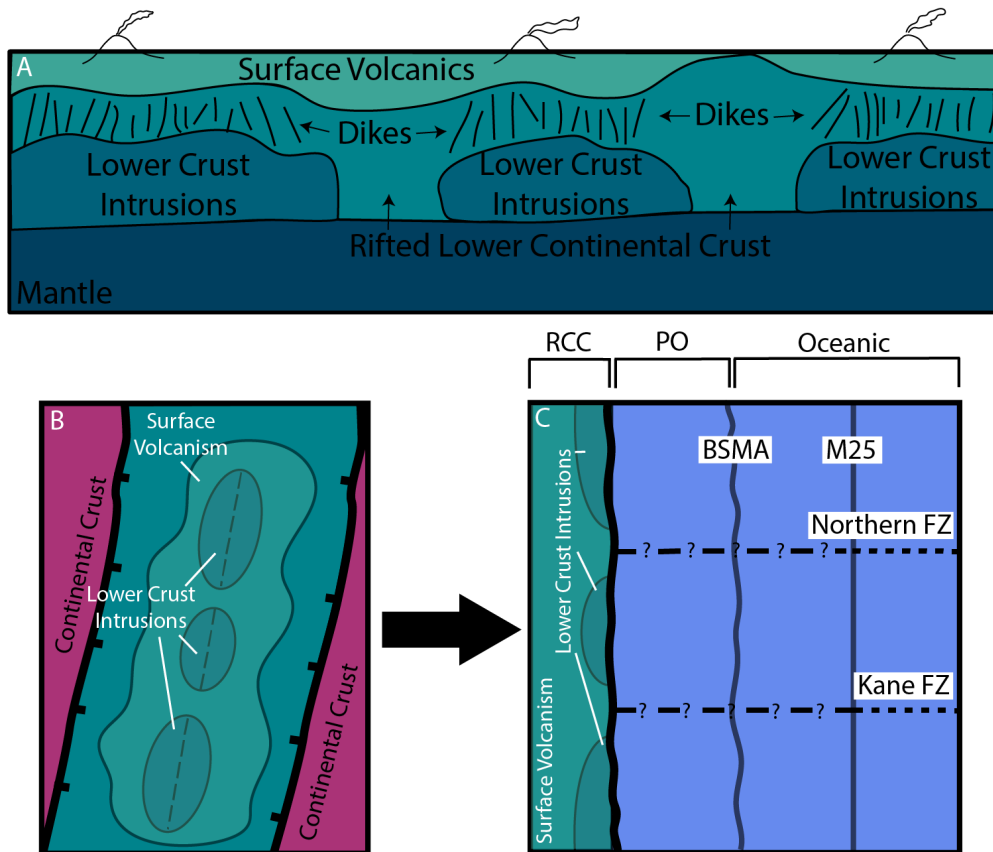
476 Our interpretation that there are variable degrees of intrusion beneath the ECMA
477 provides evidence for along-strike magmatic segmentation during the rifting process
478 (Figs. 6,7). We suggest that there were discrete sites of magmatic intrusion in the
479 continental rift that correlate to the areas with HVLC while gaps between the magmatic
480 centers remained unintruded (Fig. 7). Extensive volcanism covered the rift surface,
481 sometimes flowing away from the magmatic centers to cover the unintruded crust,
482 which is imaged now as the volcanic upper crust (Figs. 3,6,7).



483 Figure 6) **Interpretation of the Crust.** Conceptual model of the along-strike geology beneath the
484 ECMA with interpreted velocity models structures. The along-strike velocity model's crust layer is
485 comprised of a volcanic package and intrusions into the lower crust (HVLC) with diking in between
486 following interpretation by Bécél et al., (2020). HVLC gaps in the velocity model are interpreted as
487 rifted lower continental crust with no intrusion.

488 Magmatic segmentation has been observed in the active Main Ethiopian Rift and
489 in the Afar Rift where significant volcanism and crustal intrusion occur in ~30 km to
490 ~100 km long and ~20 km wide segments near the rift axis (Ebinger & Casey, 2001;
Hammond et al., 2011; Hayward & Ebinger, 1996; Keranen et al., 2004). Velocities at

491 the ENAM are faster than in the East African Rift, perhaps reflective of more mature
 492 crust with more significant magmatism at the ENAM (Hammond et al., 2011; Keranen et
 493 al., 2004). Segmentation during early-stage rifting may also manifest by border faults,
 494 some of which alternate in polarity, such as at the Midcontinent Rift or in the Malawi Rift
 495 (Dickas et al., 1997; Scholz et al., 2020). Border-fault-defined segmentation may be
 496 abandoned when magmatism and magmatic volatiles become involved and/or
 497 extension migrates to other fault systems (e.g. Ebinger & Casey, 2001; Muirhead et al.,
 498 2016).



499
 500 Figure 7) **Conceptual segmentation model.** A) A hypothetical cross section beneath the active
 501 continental rift with developed magmatic segmentation (discontinuous lower crust intrusions) and
 502 surface volcanics. B) Map view of the magmatic segmentation in the continental rift. C) The continental
 rift evolved into the Mid-Atlantic Ridge with successful breakup, and the correlation of fracture zones
 to the discontinuous HVLC gaps suggest a rift to ridge connection, but the fracture zones cannot be
 traced directly to the ECMA. BSMA is Blake Spur Magnetic Anomaly. RCC is rifted continental crust. PO
 is proto-oceanic crust defined by Shuck et al., (2019).

503

504 The cause of magmatic segmentation at the ENAM is unclear. In some locations
505 segmentation may be driven by pre-existing structures that serve as zones of
506 weakness, facilitating extension and magmatism (Frizon de Lamotte et al., 2015). The
507 ENAM has experienced multiple Wilson cycles and exhibits evidence pointing to
508 structural controls on segmentation (Thomas, 2006). However, in our study area, the
509 segmentation we observe does not appear to correlate with pre-existing structures,
510 including a suture zone and onshore basement arches (Figs. 1,3). Magmatic
511 segmentation may also be driven by small scale convection in the upper mantle,
512 providing a source of heat to weaken the lithosphere and a source of melt for
513 magmatism (Gac & Geoffroy, 2009; Geoffroy et al., 2001). It is unclear if this would
514 allow for the small-scale gaps we observe in the lower crust, or if it is more related to
515 longer wavelength segmentation.

516 Notably, the observed along-strike variations in lower crustal structure are
517 coincident with the westward extent of extrapolated fracture zones from the Mid-Atlantic
518 Ridge, which indicates a possible connection between rift and ridge segmentation (Behn
519 and Lin, 2000; Greene et al., 2017) (Figs. 3,4,7). Petrological-thermomechanical
520 modeling from some passive margins and active rifts suggests that magmatism drives
521 segmentation and that the rift segments can evolve directly into spreading segment, but
522 it is unclear if this process occurred at the ENAM or the spatial correlation is a
523 coincidence (Gerya, 2013; Illsley-Kemp et al., 2018; Taylor et al., 2009). The lack of
524 fracture zone identification between M25 and the ECMA, excluding the faint lineation
525 offsets observed by Greene et al. (2017), and the lack of correlated structures at the

526 BSMA (Shuck et al., 2019), make it difficult to draw a definitive conclusion (Figs. 1,7).
527 Further imaging of the ENAM, or other passive margins, may illuminate additional
528 along-strike variability in crustal structure and could provide stronger evidence of the rift
529 to ridge connection which is crucial for our continued understanding of continental
530 breakup and mid-ocean ridge formation.

531 **5. Conclusions**

532 1) New tomographically-derived seismic velocity models along the ECMA show that
533 crustal structure is significantly more variable along-strike than previously thought, with
534 most variability located in the lower crust. Two large “gaps” in HVLC are present in the
535 lower crust where velocities reach ~6.9 - 7.0 km/s above the Moho compared to ~7.3 -
536 7.5 km/s within the HVLC.

537

538 2) The average one dimensional velocity structure of the HVLC “gaps” match rifted
539 lower continental crust in velocity-depth space, indicating that these areas were not
540 intruded or were minimally intruded during breakup. Therefore, the along-strike crustal
541 structure beneath the ECMA consists of discrete regions of intrusion (the HVLC) and
542 regions with very limited intrusion (the HVLC gaps) covered by a volcanic layer.

543

544 3) The average lower crustal velocity and the estimated extrusive igneous thickness are
545 not correlated, indicating extensive surface volcanism regardless of lower crustal
546 intrusions. We estimate that the igneous thickness along-strike, calculated with linear
547 mixing, is ~2.5 km to ~6.0 km less than the than total crustal thickness.

548

549 4) The ratio of extrusive to intrusive thicknesses in the igneous crust beneath the ECMA
550 is less than previously defined by global studies and strike perpendicular profiles. Our
551 estimated ratio of 1 to $1.25 \pm .25$ lowers recent estimates of the ENAM's total volume by
552 ~48%.

553

554 5) The along-strike crustal variability is on similar scales to observations made at active
555 and failed continental rifts, implying that our observations reflect magmatic
556 segmentation during early rifting. The magmatic segmentation approximately aligns with
557 Mid-Atlantic Ridge fracture zones suggesting that segmentation of the rift could be
558 related to segmentation of the ridge, but further along-strike imaging of the ENAM is
559 needed to establish a definitive relationship.

560

561 **DATA and ACKNOWLEDGEMENTS**

562 The ENAM-CSE study area includes [traditional lands and waters](#) of [many Indigenous](#)
563 [peoples](#), including the Lumbee, Skaruhreh/Tuscarora, Hatteras, Roanoke and
564 Chesapeake territories. The data used in this analysis is freely available at the Marine
565 Geoscience Data System Portal under expedition code EN546: [https://www.marine-](https://www.marine-geo.org/tools/search/Files.php?data_set_uid=27784)
566 [geo.org/tools/search/Files.php?data_set_uid=27784](https://www.marine-geo.org/tools/search/Files.php?data_set_uid=27784) (doi: [10.1594/IEDA/500017](https://doi.org/10.1594/IEDA/500017)). We
567 thank the principal investigators of the ENAM-CSE, the captains and crews of the R/V
568 *Langseth* and R/V *Endeavor*, and the many technicians, students and scientists that
569 contributed to the community dataset acquisition. Masako Tominaga, John Greene, and
570 Brandon Shuck provided constructive comments and discussion during preparation of

571 this manuscript. This work was supported by NSF awards OCE-1654804 to
572 Worthington, OCE-1654781 to Magnani and OCE-1654629 to Shillington.

573

574 **References**

575

576 Alsop, L. E., & Talwani, M. (1984). The east coast magnetic anomaly. *Science*,
577 226(4679), 1189–1191.

578 Aslanian, D., Gallais, F., Afilhado, A., Schnurle, P., Moulin, M., Evain, M., et al. (2021).
579 Deep structure of the Pará-Maranhão/Barreirinhas passive margin in the equatorial
580 Atlantic (NE Brazil). *Journal of South American Earth Sciences*, 110(December
581 2020), 103322. <https://doi.org/10.1016/j.jsames.2021.103322>

582 Austin, J. A., Stoffa, P. L., Phillips, J. D., Oh, J., Sawyer, D. S., Purdy, G. M., et al.
583 (1990). Crustal structure of the Southeast Georgia embayment-Carolina trough:
584 Preliminary results of a composite seismic image of a continental suture (?) and a
585 volcanic passive margin. *Geology*, 18(10), 1023–1027.

586 Bastow, I. D., & Keir, D. (2011). The protracted development of the continent–ocean
587 transition in Afar. *Nature Geoscience*, 4(4), 248–250.

588 Bécel, A., Davis, J. K., Gibson, J. C., Shuck, B. D., Van Avendonk, H. J. A., & Gibson, J.
589 C. (2020). Evidence for a Prolonged Continental Breakup resulting from Slow
590 Extension Rates at the Eastern North American Volcanic Rifted Margin. *Journal of*
591 *Geophysical Research: Solid Earth*, e2020JB020093.
592 <https://doi.org/10.1029/2020JB020093>

593 Becker, K., Franke, D., Trumbull, R., Schnabel, M., Heyde, I., Schreckenberger, B., et
594 al. (2014). Asymmetry of high-velocity lower crust on the South Atlantic rifted
595 margins and implications for the interplay of magmatism and tectonics in
596 continental breakup. *Solid Earth*, 5(2), 1011–1026.

597 Behn, M. D., & Lin, J. (2000). Segmentation in gravity and magnetic anomalies along
598 the US East Coast passive margin: Implications for incipient structure of the
599 oceanic lithosphere. *Journal of Geophysical Research: Solid Earth*, 105(B11),
600 25769–25790.

601 Bialas, R. W., Buck, W. R., & Qin, R. (2010). How much magma is required to rift a
602 continent? *Earth and Planetary Science Letters*, 292(1–2), 68–78.

603 Biari, Y., Klingelhoefer, F., Sahabi, M., Funck, T., Benabdellouahed, M., Schnabel, M.,
604 et al. (2017). Opening of the central Atlantic Ocean: implications for geometric
605 rifting and asymmetric initial seafloor spreading after continental breakup.
606 *Tectonics*, 36(6), 1129–1150.

607 Buck, R. (2006). The role of magma in the development of the Afro-Arabian Rift System.
608 *Geological Society, London, Special Publications*, 43–54.
609 <https://doi.org/10.1144/GSL.SP.2006.259.01.05>

610 Christensen, N. I., & Mooney, W. D. (1995). Seismic velocity structure and composition
611 of the continental crust: A global view. *Journal of Geophysical Research: Solid*
612 *Earth*, 100(B6), 9761–9788.

613 Contrucci, I., Matias, L., Moulin, M., Géli, L., Klingelhoefer, F., Nouzé, H., et al. (2004).

614 Deep structure of the West African continental margin (Congo, Zaire, Angola),
615 between 5 S and 8 S, from reflection/refraction seismics and gravity data.
616 *Geophysical Journal International*, 158(2), 529–553.

617 Davis, J. K., Bécel, A., & Buck, W. R. (2018). Estimating emplacement rates for
618 seaward-dipping reflectors associated with the US East Coast Magnetic Anomaly.
619 *Geophysical Journal International*, 215(3), 1594–1603.

620 Dickas, A. B., Mudrey, M. G., Ojakangas, R. W., & Green, J. C. (1997). Segmented
621 structure of the middle Proterozoic Midcontinent rift system, North America.
622 *SPECIAL PAPERS-GEOLOGICAL SOCIETY OF AMERICA*, 37–46.

623 Dillon, W. P., Popenoe, P., Grow, J. A., Klitgord, K. D., Swift, B. A., Paull, C. K., &
624 Cashman, K. V. (1982). Growth Faulting and Salt Diapirism: Their Relationship and
625 Control in the Carolina Trough, Eastern North America: Rifted Margins: Field
626 Investigations of Margin Structure and Stratigraphy.

627 Ebinger, C., & Casey, M. (2001). Continental breakup in magmatic provinces: An
628 Ethiopian example. *Geology*, 29(6), 527–530.

629 Eddy, D. R., Van Avendonk, H. J. A., Christeson, G. L., Norton, I. O., Karner, G. D.,
630 Johnson, C. A., & Snedden, J. W. (2014). Deep crustal structure of the
631 northeastern Gulf of Mexico: Implications for rift evolution and seafloor spreading.
632 *Journal of Geophysical Research: Solid Earth*, 119(9), 6802–6822.

633 Elling, R. P., Stein, S., Stein, C. A., & Keller, G. R. (2020). Tectonic implications of the
634 gravity signatures of the Midcontinent Rift and Grenville Front. *Tectonophysics*,
635 778, 228369.

636 Faleide, J. I., Tsikalas, F., Breivik, A. J., Mjelde, R., Ritzmann, O., Engen, O., et al.
637 (2008). Structure and evolution of the continental margin off Norway and the
638 Barents Sea. *Episodes*, 31(1), 82–91.

639 Franke, D., Neben, S., Ladage, S., Schreckenberger, B., & Hinz, K. (2007). Margin
640 segmentation and volcano-tectonic architecture along the volcanic margin off
641 Argentina/Uruguay, South Atlantic. *Marine Geology*, 244(1–4), 46–67.

642 Frizon de Lamotte, D., Fourdan, B., Leleu, S., Leparmentier, F., & de Clarens, P.
643 (2015). Style of rifting and the stages of Pangea breakup. *Tectonics*, 34(5), 1009–
644 1029.

645 Gac, S., & Geoffroy, L. (2009). 3D Thermo-mechanical modelling of a stretched
646 continental lithosphere containing localized low-viscosity anomalies (the soft-point
647 theory of plate break-up). *Tectonophysics*, 468(1–4), 158–168.

648 Gallahue, M. M., Stein, S., Stein, C. A., Jurdy, D., Barklage, M., & Rooney, T. O. (2020).
649 A compilation of igneous rock volumes at volcanic passive continental margins from
650 interpreted seismic profiles. *Marine and Petroleum Geology*, 122(August), 104635.
651 <https://doi.org/10.1016/j.marpetgeo.2020.104635>

652 Geoffroy, L., Callot, J., Scaillet, S., Skuce, A., Gélard, J. P., Ravilly, M., et al. (2001).
653 Southeast Baffin volcanic margin and the North American-Greenland plate
654 separation. *Tectonics*, 20(4), 566–584.

655 Geoffroy, L., Burov, E. B., & Werner, P. (2015). Volcanic passive margins: another way
656 to break up continents. *Scientific Reports*, 5(1), 1–12.

657 Gerya, T. V. (2013). Initiation of transform faults at rifted continental margins: 3D
658 petrological-thermomechanical modeling and comparison to the Woodlark Basin.
659 *Petrology*, 21(6), 550–560.

- 660 Gerya, Taras V. (2013). Three-dimensional thermomechanical modeling of oceanic
661 spreading initiation and evolution. *Physics of the Earth and Planetary Interiors*, 214,
662 35–52.
- 663 Greene, J. A., Tominaga, M., Miller, N. C., Hutchinson, D. R., & Karl, M. R. (2017).
664 Refining the Formation and Early Evolution of the Eastern North American Margin:
665 New Insights From Multiscale Magnetic Anomaly Analyses. *Journal of Geophysical*
666 *Research: Solid Earth*. <https://doi.org/10.1002/2017JB014308>
- 667 Greene, J. A., Tominaga, M., & Miller, N. C. (2020). Along-Margin Variations in Breakup
668 Volcanism at the Eastern North American Margin. *Journal of Geophysical*
669 *Research: Solid Earth*, e2020JB020040. <https://doi.org/10.1029/2020JB020040>
- 670 Hammond, J. O. S., Kendall, J., Stuart, G. W., Keir, D., Ebinger, C., Ayele, A., &
671 Belachew, M. (2011). The nature of the crust beneath the Afar triple junction:
672 Evidence from receiver functions. *Geochemistry, Geophysics, Geosystems*, 12(12).
673 <https://doi.org/10.1029/2011GC003738>
- 674 Hayward, N. J., & Ebinger, C. J. (1996). Variations in the along-axis segmentation of the
675 Afar Rift system. *Tectonics*, 15(2), 244–257.
- 676 Holbrook, & Kelemen, P. B. (1993). Large igneous province on the US Atlantic margin
677 and implications for magmatism during continental breakup. *Nature*, 364(6436),
678 433.
- 679 Illsley-Kemp, F., Bull, J. M., Keir, D., Gerya, T., Pagli, C., Gernon, T., et al. (2018).
680 Initiation of a proto-transform fault prior to seafloor spreading. *Geochemistry,*
681 *Geophysics, Geosystems*, 19(12), 4744–4756.
682 <https://doi.org/10.1029/2018GC007947>
- 683 Keranen, K., Klemperer, S. L., Gloaguen, R., & Group, E. W. (2004). Three-dimensional
684 seismic imaging of a protoridge axis in the Main Ethiopian rift. *Geology*, 32(11),
685 949–952.
- 686 Klingelhoefer, F., Labails, C., Cosquer, E., Rouzo, S., Geli, L., Aslanian, D., et al.
687 (2009). Crustal structure of the SW-Moroccan margin from wide-angle and
688 reflection seismic data (the DAKHLA experiment) Part A: Wide-angle seismic
689 models. *Tectonophysics*, 468(1–4), 63–82.
690 <https://doi.org/10.1016/j.tecto.2008.07.022>
- 691 Klitgord, K. D., & Schouten, H. (1986). Plate kinematics of the central Atlantic. *The*
692 *Western North Atlantic Region*.
- 693 Koopmann, H., Franke, D., Schreckenberger, B., Schulz, H., Hartwig, A., Stollhofen, H.,
694 & di Primio, R. (2014). Segmentation and volcano-tectonic characteristics along the
695 SW African continental margin, South Atlantic, as derived from multichannel
696 seismic and potential field data. *Marine and Petroleum Geology*, 50, 22–39.
- 697 Korenaga, J., Kelemen, P. B., & Holbrook, W. S. (2002). Methods for resolving the
698 origin of large igneous provinces from crustal seismology. *Journal of Geophysical*
699 *Research: Solid Earth*, 107(B9), ECV-1.
- 700 LASE Study Group, L. S. (1986). Deep structure of the US East Coast passive margin
701 from large aperture seismic experiments (LASE). *Marine and Petroleum Geology*,
702 3(3), 234–242.
- 703 Luckie, T. W. (2017). Insights on magmatic addition beneath the mid-Atlantic Coastal
704 Plain from crustal seismic refraction data.
- 705 Lynner, C., Van Avendonk, H. J. A., Bécél, A., Christeson, G. L., Dugan, B., Gaherty, J.

706 B., et al. (2019). The Eastern North American Margin Community Seismic
707 Experiment: An Amphibious Active-and Passive-Source Dataset. *Seismological*
708 *Research Letters*.

709 Marzen, R. E., Shillington, D. J., Lizarralde, D., Knapp, J. H., Heffner, D. M., Davis, J.
710 K., & Harder, S. H. (2020). Limited and localized magmatism in the Central Atlantic
711 Magmatic Province. *Nature Communications*, *11*(1), 1–8.
712 <https://doi.org/10.1038/s41467-020-17193-6>

713 Marzoli, A., Callegaro, S., Dal Corso, J., Davies, J. H. F. L., Chiaradia, M., Youbi, N., et
714 al. (2018). The Central Atlantic magmatic province (CAMP): a review. In *The Late*
715 *Triassic World* (pp. 91–125). Springer. <https://doi.org/10.1007/978-3-319-68009-5>

716 Muirhead, J. D., Kattenhorn, S. A., Lee, H., Mana, S., Turrin, B. D., Fischer, T. P., et al.
717 (2016). Evolution of upper crustal faulting assisted by magmatic volatile release
718 during early-stage continental rift development in the East African Rift. *Geosphere*,
719 *12*(6), 1670–1700.

720 Museur, T., Graindorge, D., Klingelhoefer, F., Roest, W. R., Basile, C., Loncke, L., &
721 Sapin, F. (2021). Deep structure of the Demerara Plateau: From a volcanic margin
722 to a Transform Marginal Plateau. *Tectonophysics*, *803*, 228645.

723 Reuber, K. R., Pindell, J., & Horn, B. W. (2016). Demerara Rise, offshore Suriname:
724 Magma-rich segment of the Central Atlantic Ocean, and conjugate to the Bahamas
725 hot spot. *Interpretation*, *4*(2), T141–T155.

726 Scholz, C. A., Shillington, D. J., Wright, L. J. M., Accardo, N., Gaherty, J. B., &
727 Chindandali, P. (2020). Intrarift fault fabric, segmentation, and basin evolution of
728 the Lake Malawi (Nyasa) Rift, East Africa. *Geosphere*, *16*(5), 1293–1311.

729 Schouten, H., Klitgord, K. D., & Whitehead, J. A. (1985). Segmentation of mid-ocean
730 ridges. *Nature*, *317*(6034), 225–229.

731 Shillington, D., Bécel, A., Hornbach, M., Lizarralde, D., Magnani, M. B., Van Avendonk,
732 H., et al. (2014). Processed multichannel seismic data off North Carolina and
733 Virginia, acquired during R/V Marcus G. Langseth expedition MGL1408 (2014) as
734 part of the Eastern North America Community Seismic Experiment (ENAM).
735 Interdisciplinary Earth Data Alliance (IEDA), doi.

736 Shuck, B., Van Avendonk, H. J. A., & Bécel, A. (2019). The role of mantle melts in the
737 transition from rifting to seafloor spreading offshore eastern North America. *Earth*
738 *and Planetary Science Letters*, *525*, 115756.

739 Taylor, B., Goodliffe, A., Martinez, F., & Hey, R. (1995). Continental rifting and initial
740 sea-floor spreading in the Woodlark Basin. *Nature*, *374*(6522), 534–537.

741 Taylor, B., Goodliffe, A., & Martinez, F. (2009). Initiation of transform faults at rifted
742 continental margins. *Comptes Rendus Geoscience*, *341*(5), 428–438.

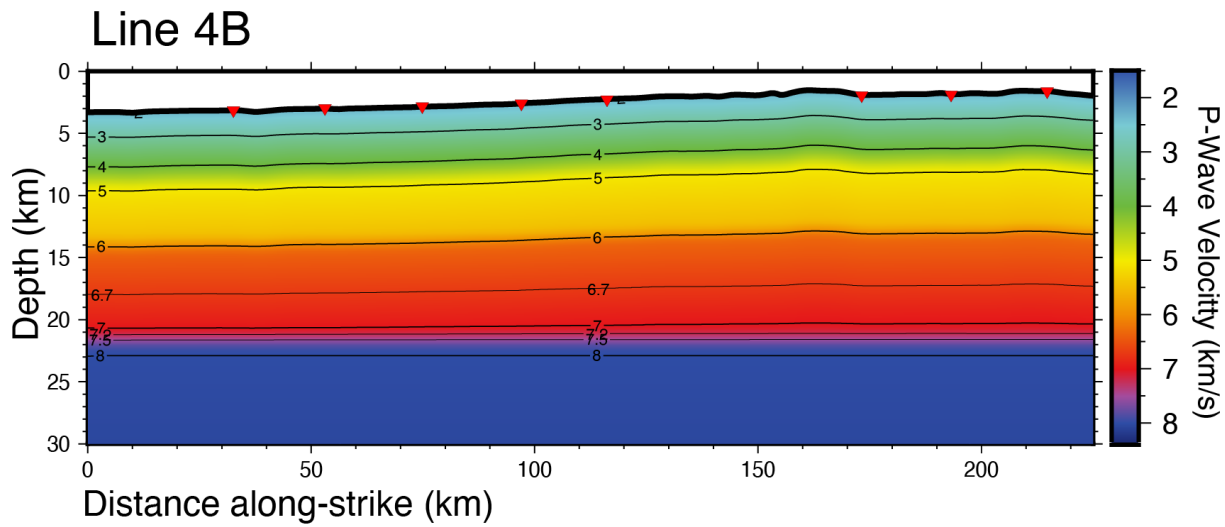
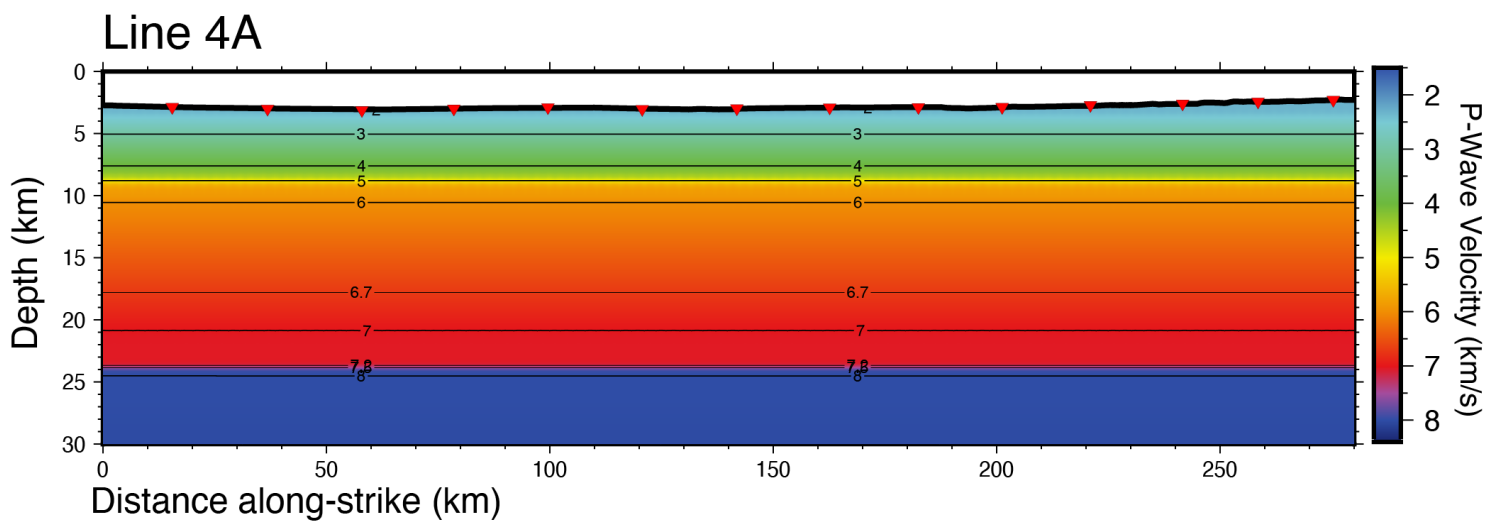
743 Thomas, W. A. (2006). Tectonic inheritance at a continental margin. *GSA Today*, *16*(2),
744 4–11.

745 Thybo, H., & Nielsen, C. A. (2009). Magma-compensated crustal thinning in continental
746 rift zones. *Nature*, *457*(7231), 873–876.

747 Thybo, Hans, & Artemieva, I. M. (2013). Moho and magmatic underplating in continental
748 lithosphere. *Tectonophysics*, *609*, 605–619.

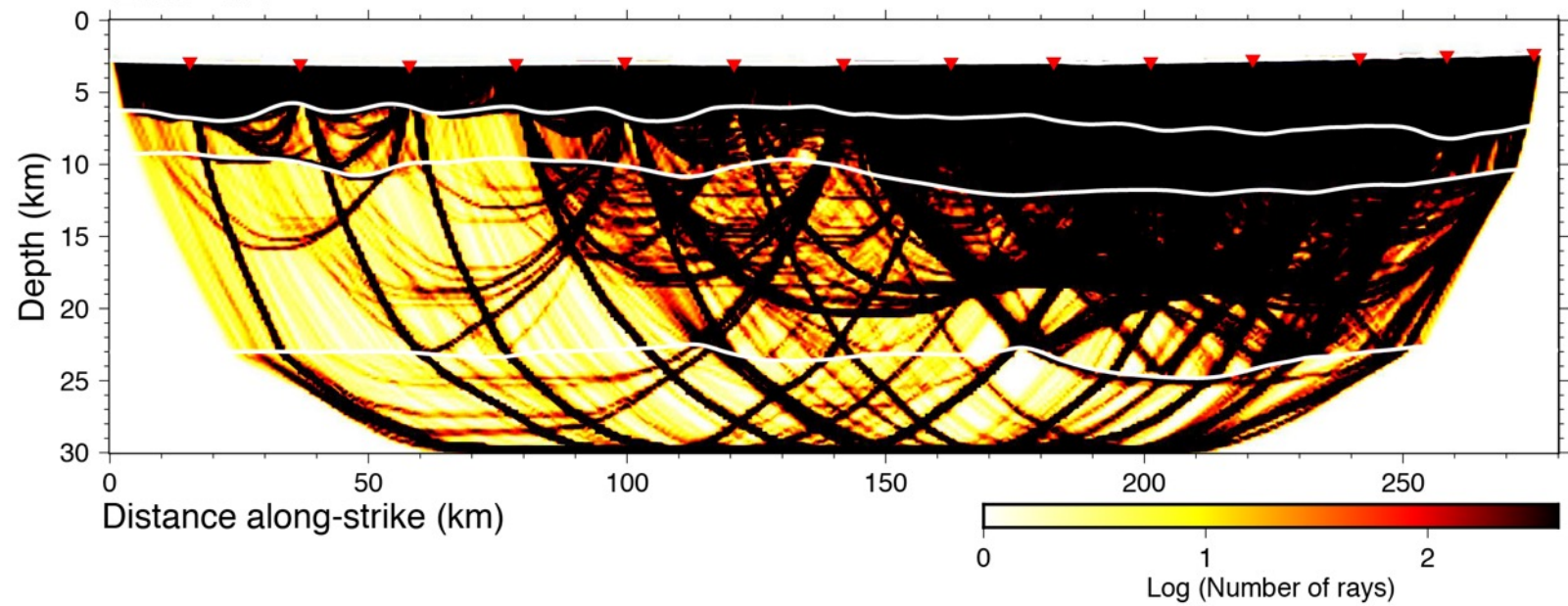
749 Tréhu, A. M., Ballard, A., Dorman, L. M., Gettrust, J. F., Klitgord, K. D., & Schreiner, A.
750 (1989). Structure of the lower crust beneath the Carolina Trough, US Atlantic
751 continental margin. *Journal of Geophysical Research: Solid Earth*, *94*(B8), 10585–

752 10600.
753 Van Avendonk, H., Shillington, D. J., Holbrook, W. S., & Hornbach, M. J. (2004).
754 Inferring crustal structure in the Aleutian island arc from a sparse wide-angle
755 seismic data set. *Geochemistry, Geophysics, Geosystems*, 5(8).
756 Van Avendonk, H., (2015). Ocean bottom seismometer data, updated with relocated
757 instrument coordinates, off North Carolina and Virginia, acquired during R/V
758 Endeavor expedition EN546 (2014) as part of the Eastern North America
759 Community Seismic Experiment (ENAM). IEDA. doi:[10.1594/IEDA/500017](https://doi.org/10.1594/IEDA/500017)
760 White, R. S., Smith, L. K., Roberts, A. W., Christie, P. A. F., & Kusznir, N. J. (2008).
761 Lower-crustal intrusion on the North Atlantic continental margin. *Nature*, 452(7186),
762 460–464.
763 Wyer, P., & Watts, A. B. (2006). Gravity anomalies and segmentation at the East Coast,
764 USA continental margin. *Geophysical Journal International*, 166(3), 1015–1038.
765

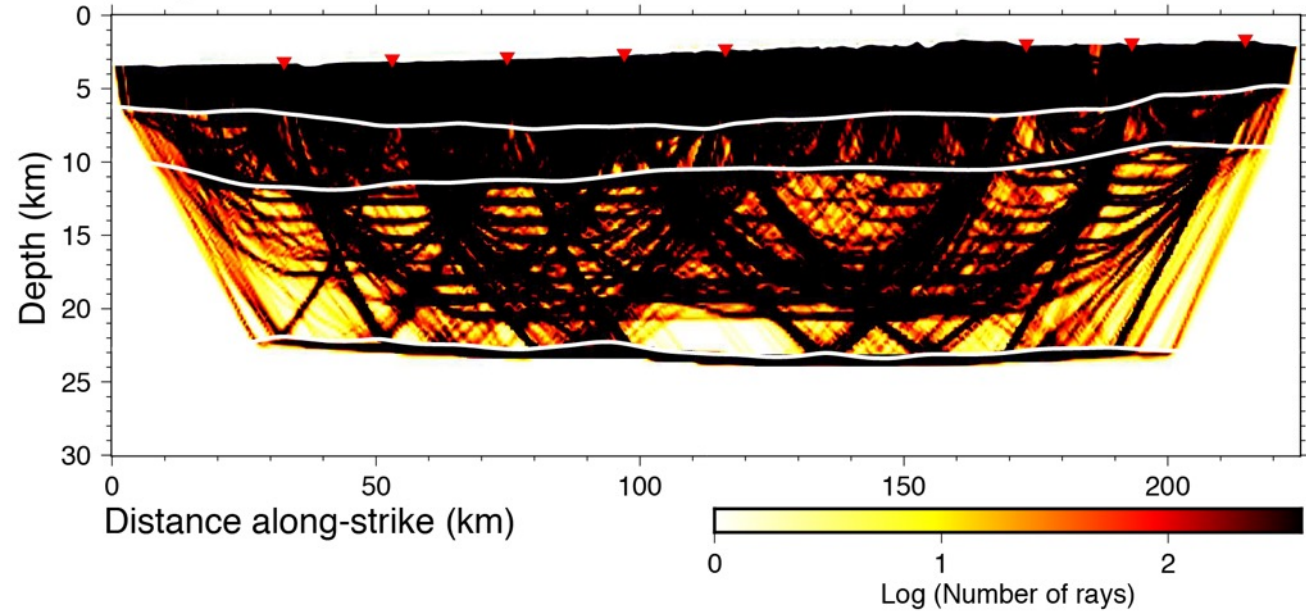


Supplemental Figure 1) **Starting models.** Starting velocity models for Line 4A (top) and Line 4 B (bottom) based on the velocity-depth profile taken from the Line 4A-Line 2 and Line 4B-Line 1 intersections (Shuck et al., 2019). One-dimensional velocity-depth profiles are shown in figure 3 inset.

Line 4A

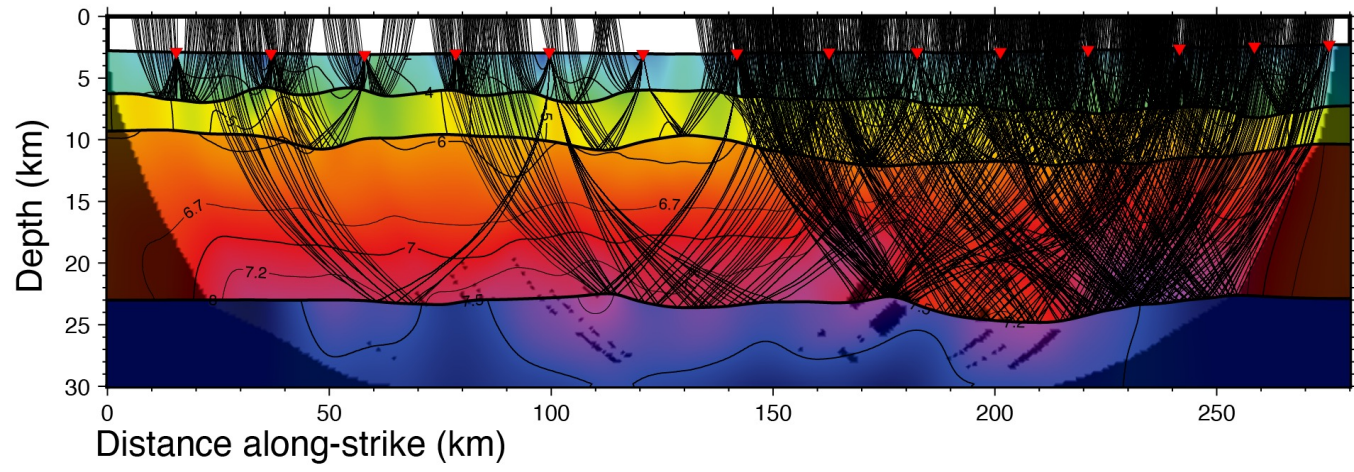


Line 4B

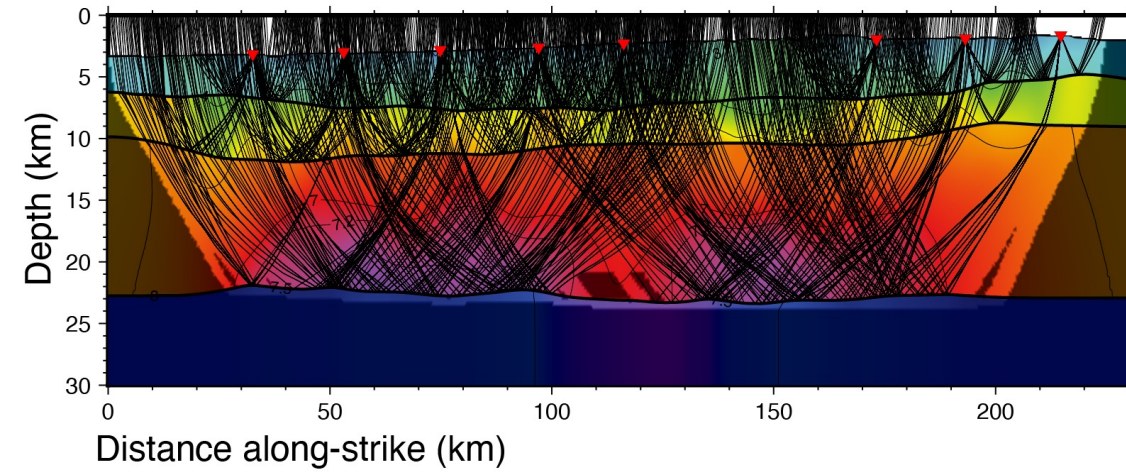


Supplemental Figure 2) **Ray coverage.** Derivative weight sum plots for line 4A (top) and 4B (bottom) showing density of ray coverage. Darker colors indicate denser ray coverage while lighter colors indicate less dense coverage. Light area between 0 and 100 km on line 4A corresponds to shallow salt diapirs that inhibit deeper arrivals for this area.

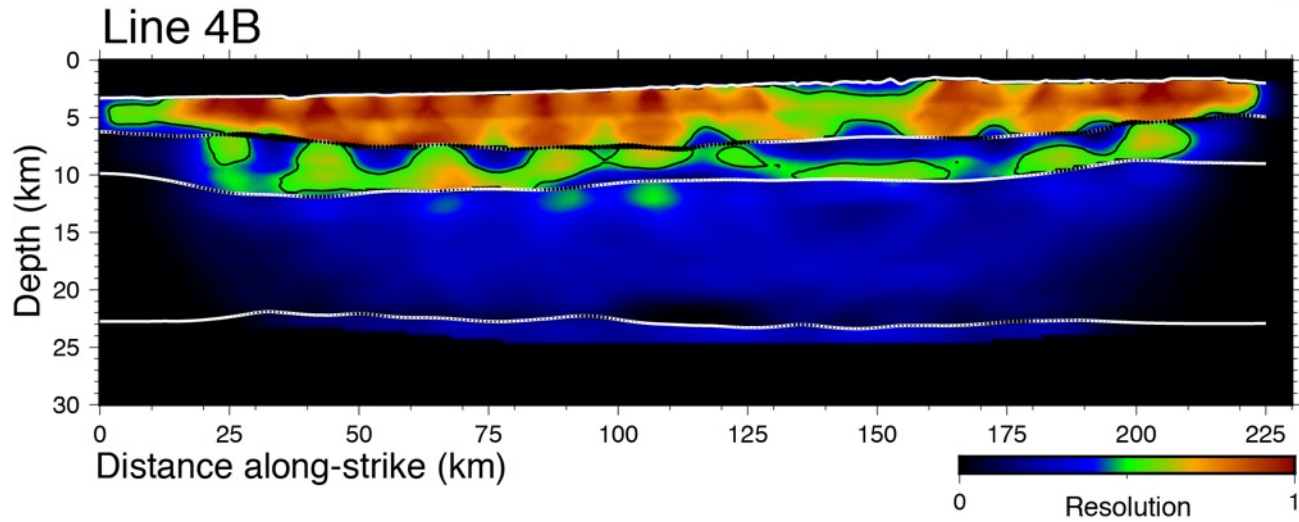
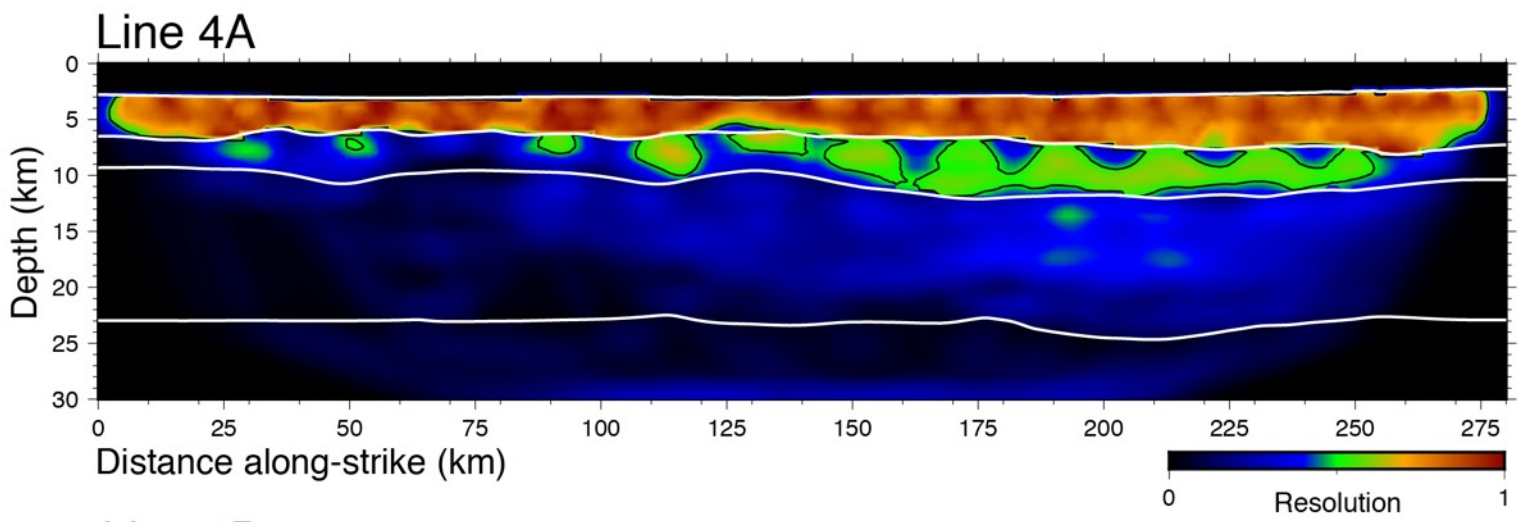
Line 4A



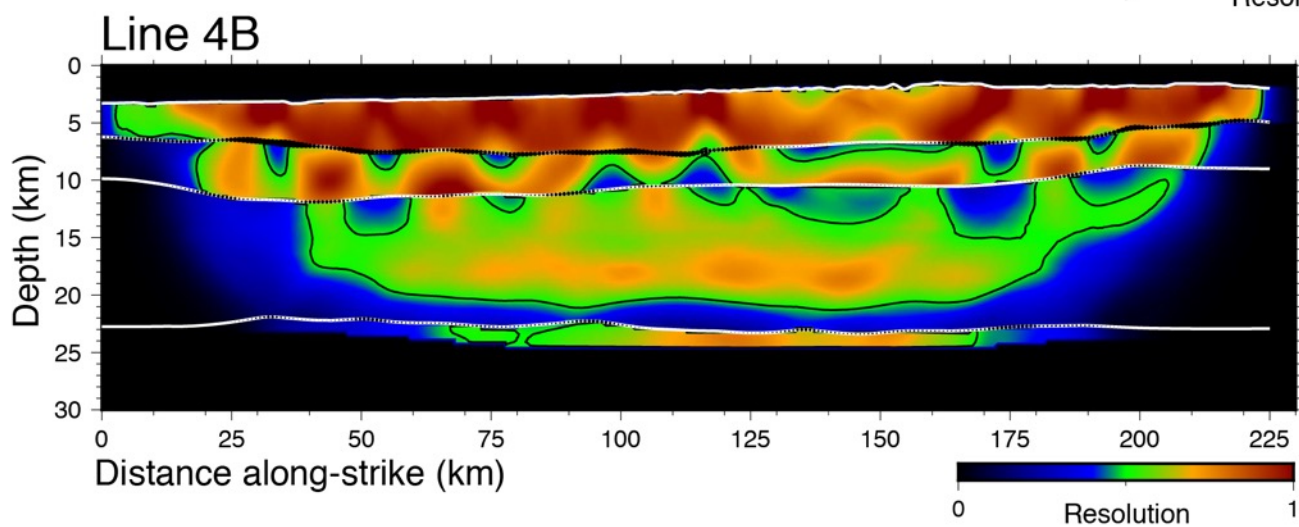
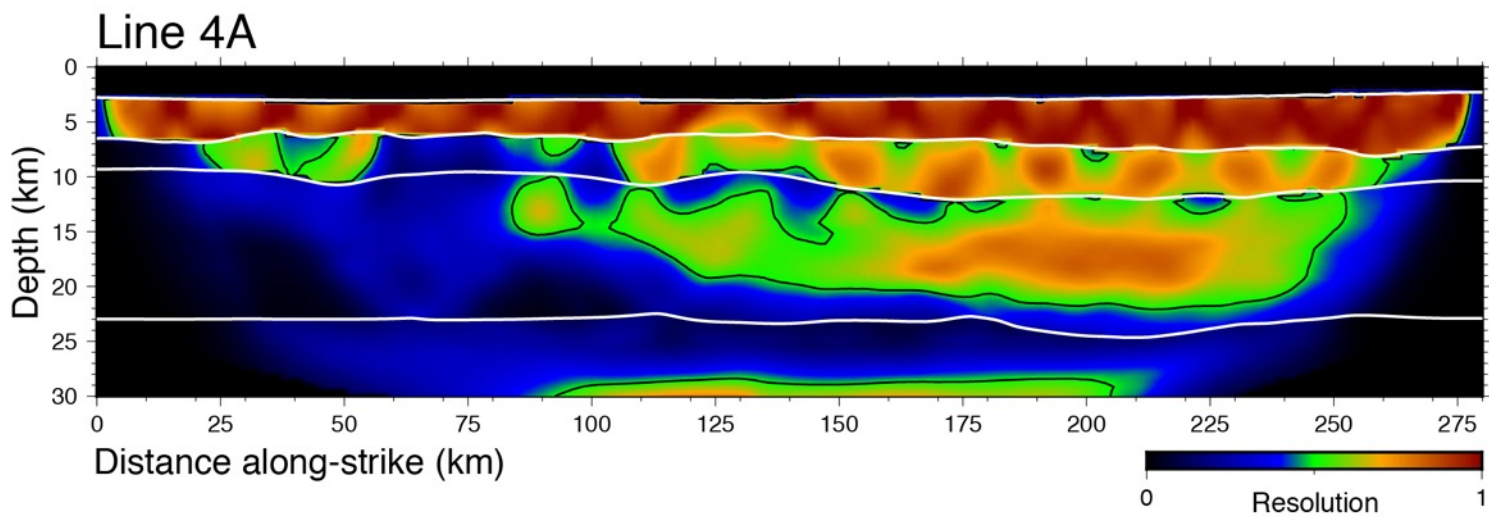
Line 4B



Supplemental Figure 3) **Wide-angle reflection ray coverage.** Raypath diagram for Line 4A (top) and Line 4B (bottom) showing only wide-angle reflections that constrain the boundary depths.

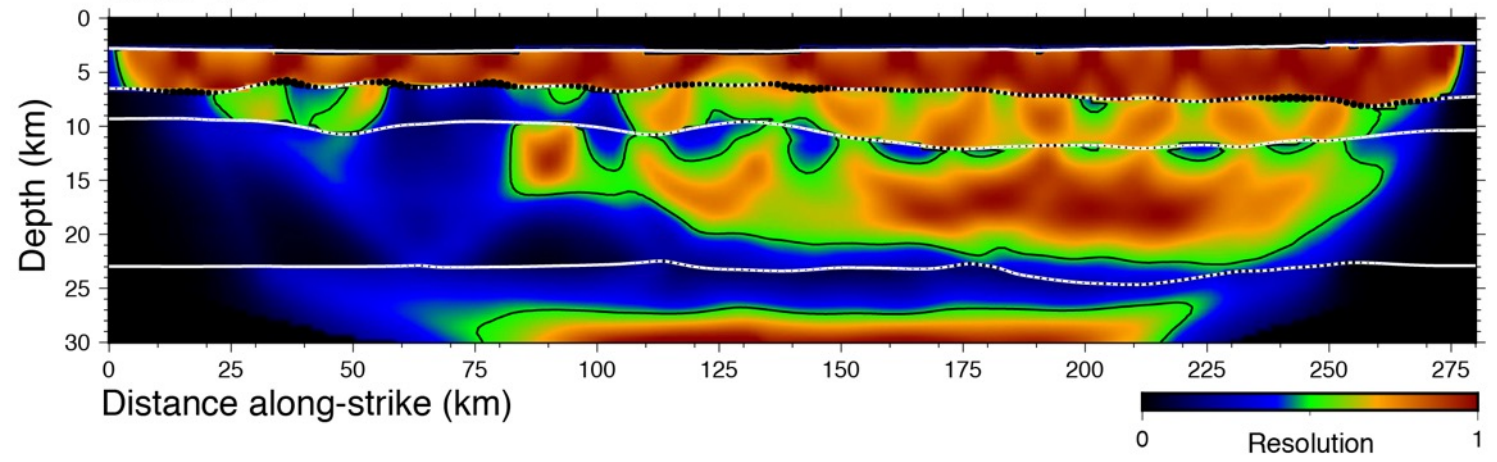


Supplemental Figure 4) **Small Object Resolution Test**. Resolution testing for line 4A (top) and 4B (bottom) with an ellipse of 10 km wide by 2 km tall. Acceptable resolution is considered greater than 50% (heavy black contour separating blue and green). Black dots on boundaries reflect constraint from wide-angle reflections.

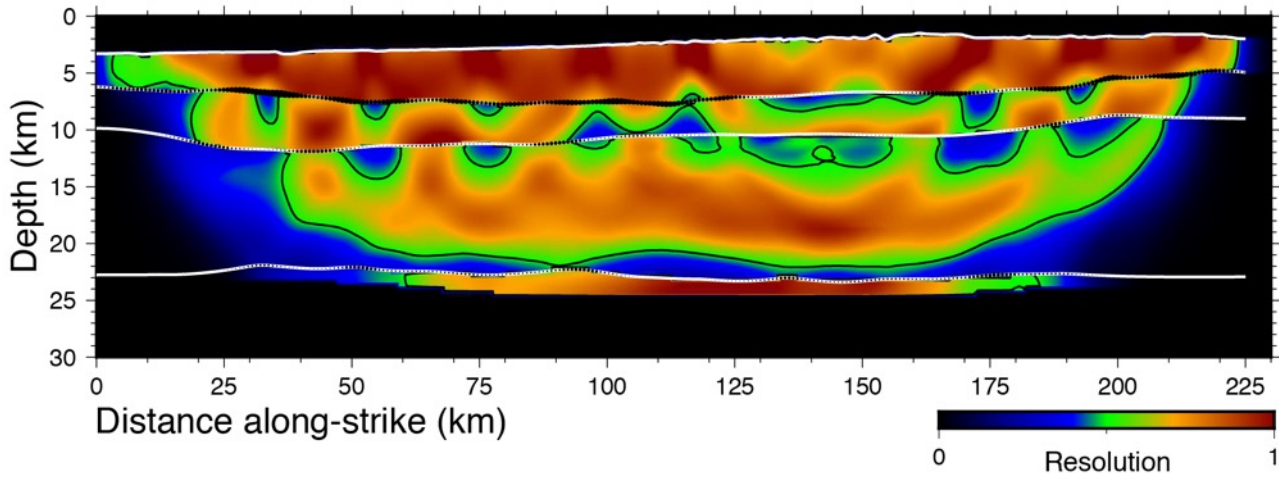


Supplemental Figure 5) **Medium Object Resolution Test.** Resolution testing for line 4A (top) and 4B (bottom) with an ellipse of 30 km wide by 5 km tall. Acceptable resolution is considered greater than 50% (heavy black contour separating blue and green). Black dots on boundaries reflect constraint from wide-angle reflections.

Line 4A

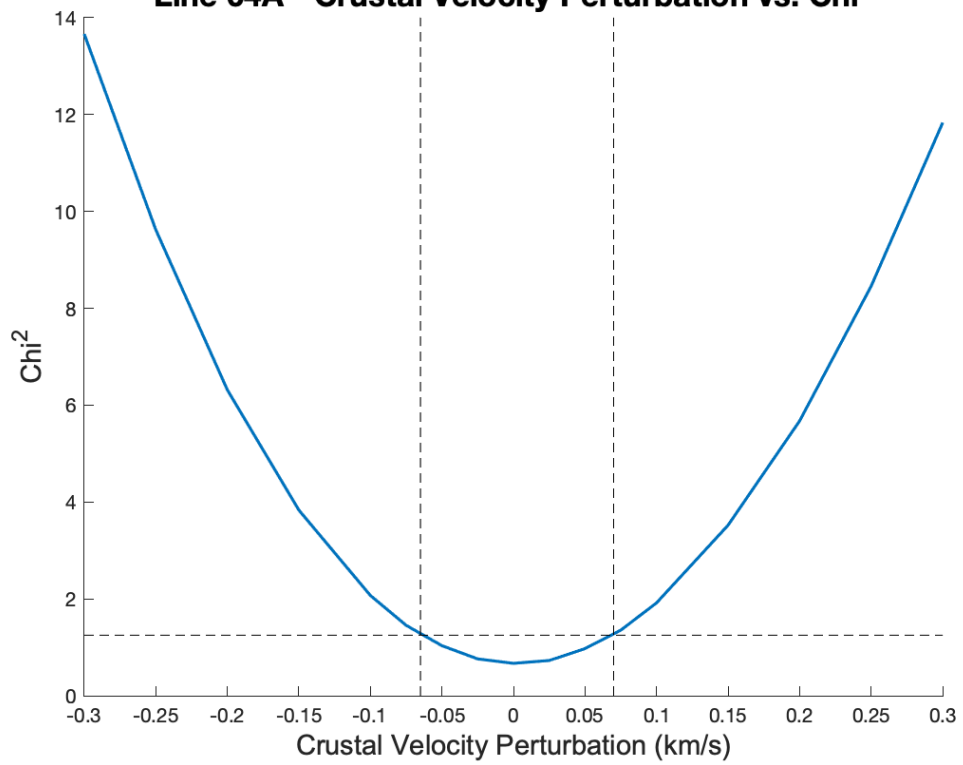


Line 4B

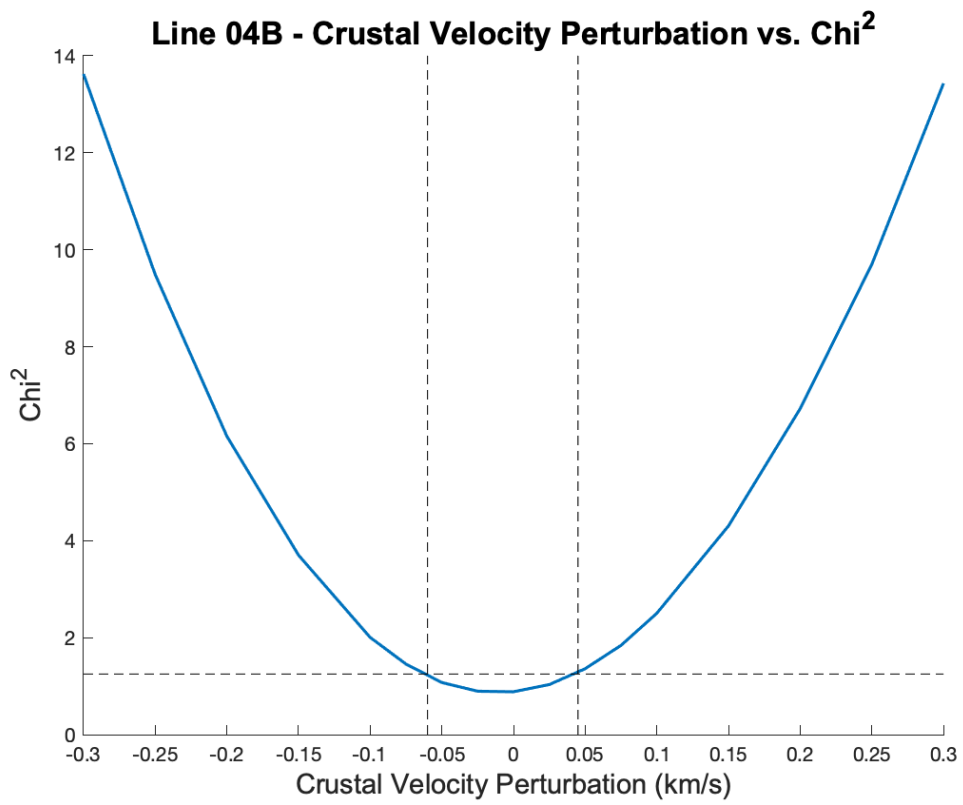


Supplemental Figure 6) **Large Object Resolution Test.** Resolution testing for line 4A (top) and 4B (bottom) with an ellipse of 60 km wide by 8 km tall. Acceptable resolution is considered greater than 50% (heavy black contour separating blue and green). Black dots on boundaries reflect constraint from wide-angle reflections.

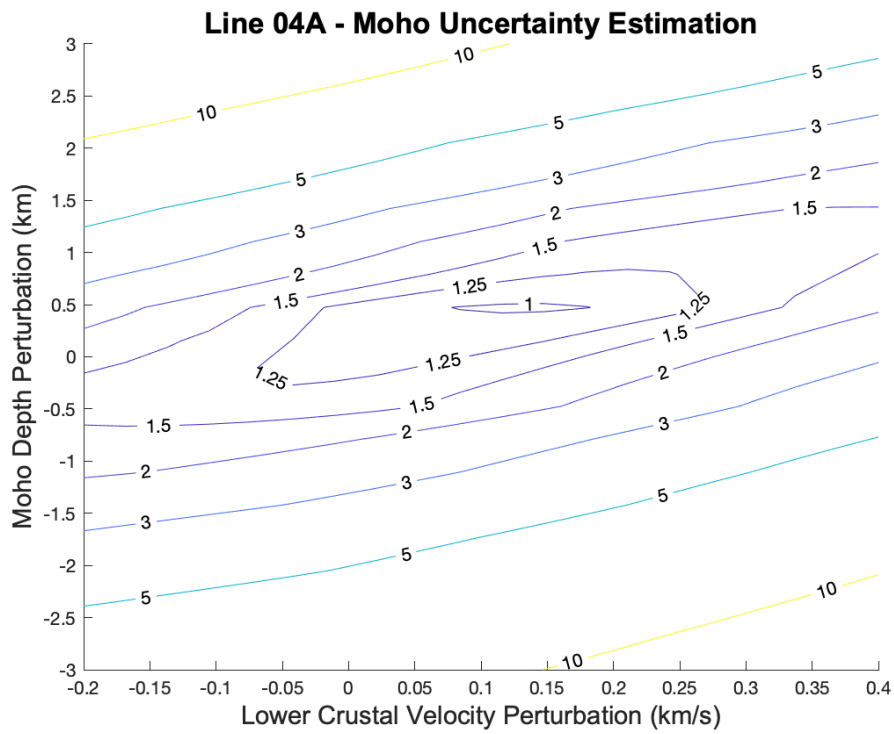
Line 04A - Crustal Velocity Perturbation vs. Chi²



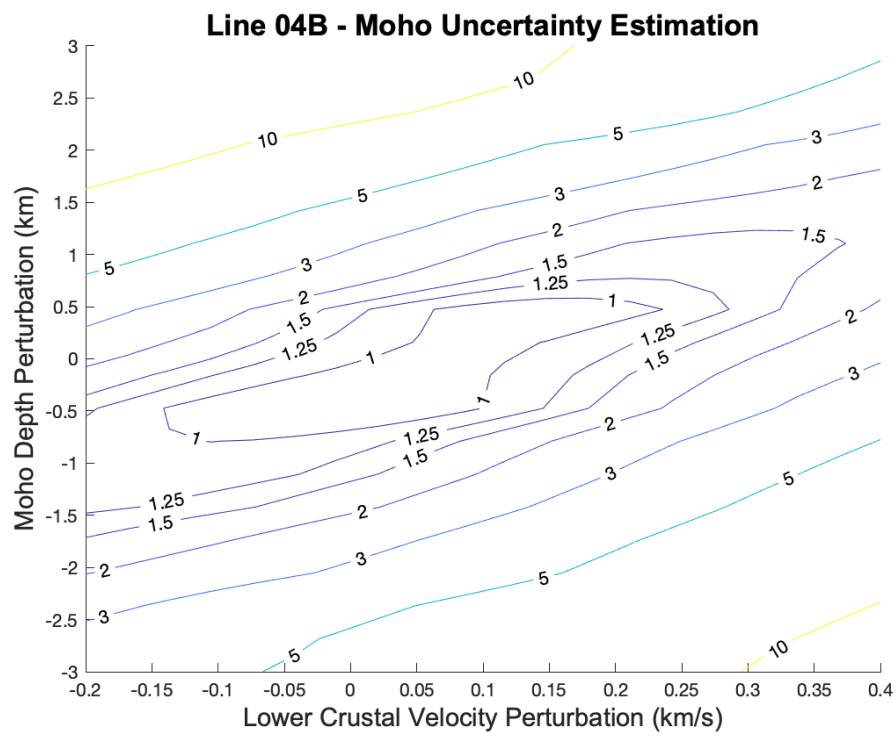
Supplemental Figure 7) **Crustal Velocity Uncertainty – Line 04A**. Testing the velocity uncertainty of Line 04A's crust layer. Velocities are perturbed by the value on the x axis, the model is raytraced only with the Pg phase, and the resulting chi² is calculated. A chi² of 1.25 (horizontal dashed line) is considered an acceptable value, which results in acceptable velocity perturbations ranging from -0.05 to 0.07 km/s (vertical dashed lines).



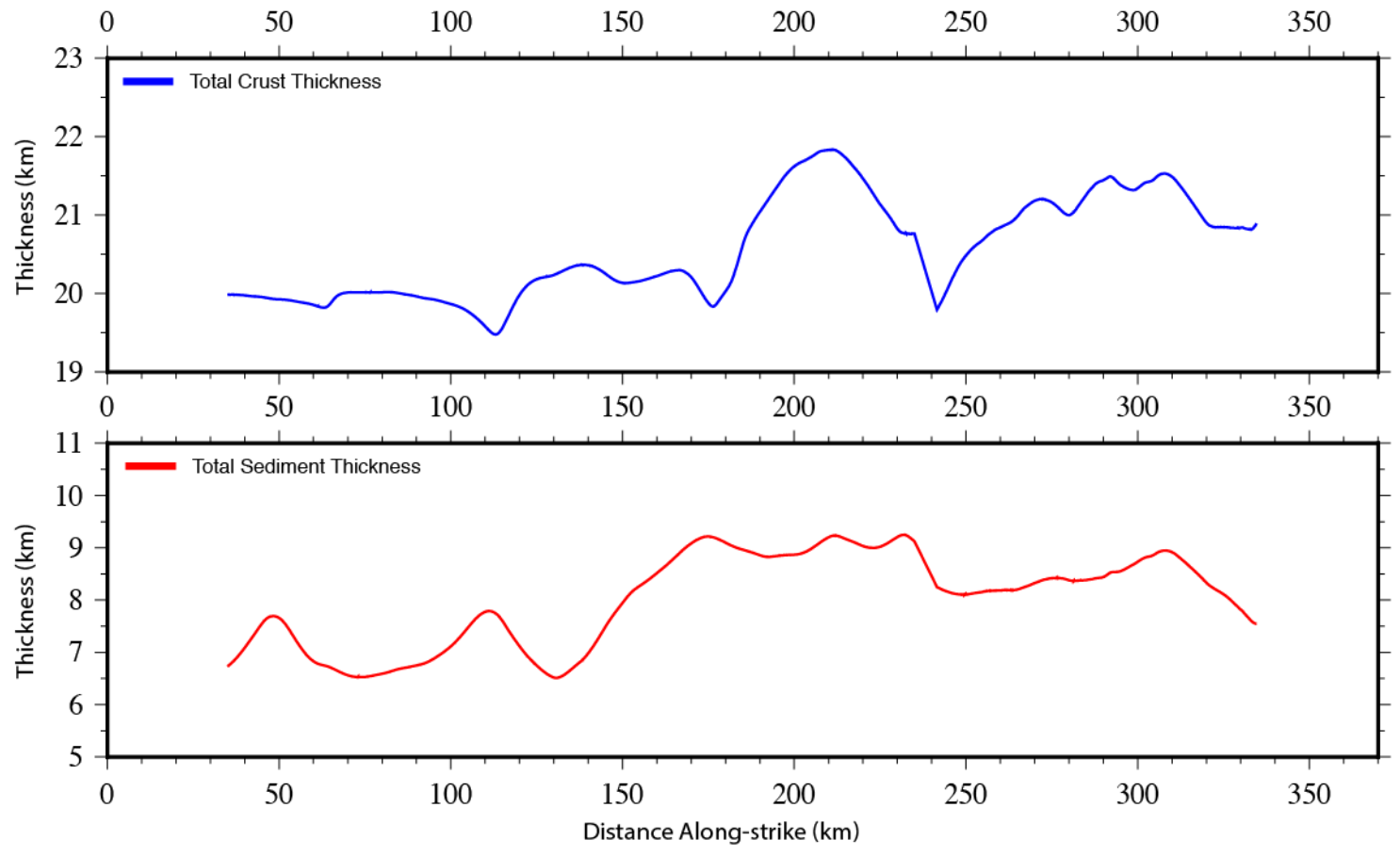
Supplemental Figure 8) **Crustal Velocity Uncertainty – Line 04B**. Testing the velocity uncertainty of Line 04B’s crust layer. Velocities are perturbed by the value on the x axis, the model is raytraced only with the Pg phase, and the resulting chi² is calculated. A chi² of 1.25 (horizontal dashed line) is considered an acceptable value, which results in acceptable velocity perturbations ranging from -0.06 to 0.045 km/s (vertical dashed lines).



Supplemental Figure 9) **Moho Uncertainty Estimation – Line 04A.** Testing the Moho velocity-depth tradeoff uncertainty of Line 04A. Velocities are perturbed by the value on the x axis and the Moho depth is perturbed by the value on the y axis. The model is then raytraced only with the PmP phase and the resulting χ^2 is calculated. A χ^2 of 1.25 is considered an acceptable value, which results in acceptable velocity perturbations ranging from -0.07 to 0.27 km/s and acceptable depth perturbations from -0.28 to 0.85 km.



Supplemental Figure 10) **Moho Uncertainty Estimation – Line 04B.** Testing the Moho velocity-depth tradeoff uncertainty of Line 04B. Velocities are perturbed by the value on the x axis and the Moho depth is perturbed by the value on the y axis. The model is then raytraced only with the PmP phase and the resulting χ^2 is calculated. A χ^2 of 1.25 is considered an acceptable value, which results in acceptable velocity perturbations ranging from -0.2 to 0.29 km/s and acceptable depth perturbations from -1.5 to 0.78 km.



Supplemental Figure 11) **Additional along-strike calculations.** *Top* – Total crustal thickness from seafloor to Moho. *Bottom* – Total sediment thickness from seafloor to top of the crust.